MULTIMODAL SEGMENTATION OF BRAIN MR IMAGES THROUGH HIDDEN MARKOV RANDOM FIELDS

by

Ufuk MAT

BS, Electrical & Electronics Engineering, Bogazici University, 2006

Submitted to the Institute of Biomedical Engineering
in partial fulfillment of the requirements
for the degree of
Master of Science
in
Biomedical Engineering

Boğaziçi University
June 2009

MULTIMODAL SEGMENTATION OF BRAIN MR IMAGES THROUGH HIDDEN MARKOV RANDOM FIELDS

APPROVED BY:

Prof. Mehmed OZKAN .....
(Thesis Advisor)

Prof. Yorgo ISTEFANOPULOS .....

Prof. Ahmet ADEMOGLU .....

DATE OF APPROVAL: 17.06.2009

ACKNOWLEDGMENTS

First of all, I would like to thank my advisor, Prof. Mehmed Ozkan, for his generous help and guidance throughout the project. He has been very supportive and encouraging during this study.

I also would like to thank Bora Buyuksarac for his guidance and support throughout my thesis, Onur Agus who had provided me with the MR data I used in this work and Zeynep Firat, MR researcher in Yeditepe University Hospital, for her help and patience during MR data acquisitions.

In addition, I would like to thank my friends G. Damla Altinok and Ozgur Dalkilic for their unlimited encouragement.

Finally, I would like to thank my family, Zafer Mat, Lutfiye Mat and Sezen Mat, for their invaluable support and encouragement. Without their support I could never make it this far.

ABSTRACT

MULTIMODAL SEGMENTATION OF BRAIN MR IMAGES THROUGH HIDDEN MARKOV RANDOM FIELDS

Segmentation of brain MR images, especially into three main tissue types: CSF, GM and WM, is an essential task in clinical applications as it aids surgical planning, computer-aided neurosurgery and diagnosis. However, every single MR image contains degenerative components such as noise and RF inhomogeneity which dramatically reduces the accuracy of the results of automatic post-processing techniques.

A number of methods are proposed in the literature for tissue segmentation of brain MR images. Among these, Otsu thresholding, ML estimation and MRF model based methods are the ones that widely used. Moreover, $2D$ segmentation of $True - T_1$ and $True - T_2$ images almost completely removes the artifacts mentioned above hence results in the best results ever reported. However, the required scan time of the method and the expence of the process makes this method inapplicable to clinical applications.

In this study, three different segmentation schemes for brain MR images, namely Otsu thresholding, ML classification and MRF model based segmentation, are analyzed taking the segmentation results of $2D$ segmented true parameter images and a novel multivariate MRF segmentation method using T_1 and T_2-weighted images is proposed.

As a result, the performance of the segmentation methods when two dimensional data were used increased. Moreover, multivariate HMRF model-based segmentation method achieved the best results.

Keywords: Magnetic resonance imaging, Otsu thresholding, ML classification, MRF theory, multivariate segmentation.

ÖZET

BEYİN MR İMGELERİNİN GİZLİ MARKOV RASGELE ALANLARIYLA ÇOK DEĞİŞKENLİ BÖLÜTLENMESİ

Beyin MR imgelerinin, özellikle üç ana doku tipi olan CSF, GM ve WM'a, bölütlenmesi, uygulamanın cerrahi planlama, bilgisayar destekli nörocerrahi ve tanıdaki katkılarından dolayı, klinik uygulamalarda vazgeçilmezdir. Bununla birlikte, her bir MR imgesi otomatik sonradan işleme tekniklerinin sonuçlarının hatasızlığını çarpıcı ölçüde düşüren gürültü ve RF inhomojenligi gibi bozucu bileşenler içermektedir.

Literatürde beyin MR imgelerinin bölütlenmesi için birtakım metotlar önerilmektedir. Bunlar arasında Otsu eşiklemesi, ML ve MRF modele dayalı metotlar en çok kullanılanlardır. Ayrıca gerçek T_1 ve T_2 görüntülerinin iki boyutlu bölütlenmesi yukarıda bahsi geçen bozulmaları neredeyse tamamen ortadan kaldırdıgı için şu ana kadar bildirilmiş en iyi sonuçları vermektedir. Fakat, metot için gereken tarama zamanı ve sürecin masrafı bu yöntemi klinik uygulamalar açısından uygunsuz kılmaktadır.

Bu çalışmada üç farklı bölütleme düzeni, sırasıyla Otsu eşiklemesi, ML sınıflandırma ve MRF modele dayalı metot, gerçek değişkenli imgelerin iki boyutlu bölütlemesi baz alınarak incelenecek, T_1 ve T_2 ağırlıklı imgeler kullanılarak yeni çok değişkenli MRF bölütlenme metodu arz edilecektir.

Sonuş olarak, iki boyutlu veri kullanımı, bölütlenme algoritmalarının başarımını arttırmıştır. Buna ek olarak, çok değişkenli HMRF model tabanlı bölütlenme en başarılı bölütlenme sonuçlarını vermiştir.

Anahtar Sözcükler: Manyetik rezonans görüntüleme, Otsu eşiklemesi, ML sınıflandırma, MRF teori, çok değişkenli bölütlenme.

TABLE OF CONTENTS

LIST OF FIGURES

LIST OF TABLES

LIST OF SYMBOLS

T_1	Spin-Lattice relaxation
T_2	Spin-Spin relaxation
T_R	Repetition time
T_E	Echo time
M_z^0	Proton density
A_E	Signal intensity
$\mathcal{L}$	State space for hidden random variables
$\mathcal{D}$	State space for observable random variables
$\mathcal{S}$	Set of indices
R	Any family of random variables
R_i	A random variable belonging to R
r_i	The value of random variable R_i
r	A configuration of R
X	Hidden random field
Y	Observable random field
$\mathbf{x}$	A configuration of random field X
$\mathbf{y}$	A configuration of random field Y
$\mathcal{X}$	Set of all possible configurations of X
$\mathcal{Y}$	Set of all possible configurations of Y
$P(\mathbf{x})$	Probability of observing the random field configuration $\mathbf{x}$
i	Index to sites
$\mathcal{N}$	Neighborhood system
$\mathcal{N}_i$	Neighbors of site i
Z	Partition function
$U(\mathbf{x})$	Energy function
c	Clique c
$\mathcal{C}$	All possible cliques
$V_c(\mathbf{x})$	Clique potential

$\hat{\mathbf{x}}$	Estimation of true label $\mathbf{x}$
Q	Cost function
t	Iteration number
$E_i(x_i)$	Conditional posterior potential for pixel i for label x_i
$S_i(x)$	The stability of i with respect to x
B	Bias field
$\hat{B}$	Estimate of bias field
b_i	Bias field at pixel i
I	Observed image
I^*	Ideal image
I_i	Observed intensity at pixel i
I_i^*	Ideal intensity at pixel i
$\mathbf{y}^*$	Ideal configuration of random field Y
y_i	Observed value of random variable y at pixel i
y_i^*	Ideal value of random variable y at pixel i
W_{ij}	Weights
j	Tissue class
θ	Parameter set for a specified probability distribution
θ_l	Parameter set for label l
ψ_B	$N \times N$ covariance matrix

LIST OF ABBREVIATIONS

MRI	Magnetic resonance imaging
NMR	Nuclear magnetic resonance
GM	Gray matter
WM	White matter
CSF	Cerebrospinal fluid
ML	Maximum likelihood
MAP	Maximum *a posteriori*
FM	Finite mixture
FGM	Finite Gaussian mixture
MRF	Markov random field
HMM	Hidden Markov model
HMRF	Hidden Markov random field
GHMRF	Gaussian hidden Markov random field
B_1	Rotating magnetic field generated by transmitter coil in MR
RF	Radio frequency
EM	Expectation Maximization
HCF	Highest Confidence First
ICM	Iterated conditional modes

1. INTRODUCTION

Magnetic Resonance Imaging (MRI) provides detailed images using nuclear magnetic resonance (NMR) principles, and is used for both brain and body human studies [1]. It has several advantages over other imaging modalities enabling it to provide three-dimensional (3D) data with high soft tissue contrast. However, amount of data is far too much for manual image analysis, and this has been one of the biggest problems in the effective use of MRI. For this reason, automatic or semi-automatic techniques of computer-aided image analysis are necessary. Segmentation of MR images into different tissue classes, especially gray matter (GM), white matter (WM) and cerebrospinal fluid (CSF), is an important task in medical applications [2]. That is because, the quantitative assessment of brain tissue volumes plays an important role in diagnosis, surgical planning, monitoring the clinical outcome and treatment effects in many diseases, such as Alzheimer disease, multiple sclerosis, schizophrenia, alcoholism and AIDS-related dementia.

A wide variety of approaches have been proposed for brain MR image segmentation, such as clustering methods, histogram-based methods, region-growing methods and the statistical ones. Among these, statistical methods, especially the parametric ones, are widely employed in the literature [3, 4]. "This type of method labels pixels according to probability values, which are determined based on intensity distribution of the image. With a suitable assumption about the distribution, statistical approaches attempt to solve the problem of estimating the associated class label, given only the intensity for each pixel. Such an estimation problem is necessarily formulated from an established criterion". Maximum *a posteriori* (MAP) or maximum likelihood (ML) principles are two such methods adopted for this kind of applications. "But before those criteria can be assessed, the formula for the density function of the pixel intensity has to be chosen carefully [5]. *Finite Mixture* (FM) models, in particular *finite Gaussian Mixture* (FGM) model when the Gaussian likelihood distribution is assumed [6, 7], is one of the most widely used models in segmentation. FM models have a number of

elegant features and are mathematically simple. However, being a histogram-based model, the FM has an intrinsic limitation - spatial information is not taken into account because all the data points are considered to be independent samples drawn from a population" [2]. Because of this limitation, the FM models work well on the images with low levels of noise; unfortunately, this is often not the case with MR images due to artifacts such as the partial volume effect and bias field distortion. Under these conditions, FM model-based methods come up with unaccurate segmentation results and any other method which resolves partial volume effects and bias field distortion problems should be considered.

In order to cope with this problems the use of HMRF models were adressed in [8, 9, 10], which are stochastic processes generated by a MRF whose state sequence cannot be observed directly but with the help of some observed values, such as pixel intensities in our context. The importance of the HMRF model derives from MRF theory, in which the spatial information in an image is encoded through the relationship among neighboring pixels. By adopting such a constraint other than just using the intenstiy values, the expectation of the neigboring pixels to be the member of the same class increases.

Further a new approach [11] addresses the degenerative effect of bias fields in MR data. In that approach one gets eight scans of the same slice for eight different parameter sets and fits a curve using the intensities of each pixel according to the theoretical intensity equation and finds global parameters, namely true-T_1's and true-T_2's. These true-T_1 and true-T_2 values for each pixel constructs true-T_1 image and true-T_2 image, respectively. All in all, the result is a 2D image from a total of eight images which eliminates the bias field effect greatly. However, the time required to get these images from the patient, and the expense of the scan makes that method unfeasible for clinical purposes. A more comprehensive explanations of the methods will be given in the next section.

Taking the aforementioned disadvantages of the methods above into account, a robust fully automatic and reliable method with a short data acquisition time is in-

evitable. The proposed method in this thesis is the use of HMRF model in segmentation with the probabilistic information coming from just two of the images corresponding to two different parameters sets. This method greatly reduces the scan time and expenses with a comparable success in segmentation results.

All the methods in this thesis were implemented in C++ using Microsoft Visual Studio 8. For reading images in DICOM format, ITK (Insight Tool Kit) was used. For the visualization of images VTK (Visualization Tool Kit) was used. These kits can be found in *www.itk.org* and *www.vtk.org*, respectively.

In Chapter-2 signal intensity artifacts on MR data, ML classification and the calculation of true parameter images will be discussed. Chapter-3 gives the mathematical background of MRF theory and HMRF models in image analysis. In Chapter-4 segmentation results corresponding to different classification algorithm will be given with the quantitative analysis of the segmented images. Chapter-5 discusses the results in detail and offers new methods for future work. Appendix-A is the proof of Levenberg-Marquardt algorithm used in the calculation of true parameters of the images and Appendix-B gives the mathematics underlying Otsu thresholding.

2. BACKGROUND

In this chapter, bias field and its effects on image and image processing techniques, ML classification and HMRF models and segmentation using true parameter images will be covered in detail.

2.1 Image Artifacts in MRI

Although being one of the most popular imaging techniques of today's technology, MR data still suffer from some signal intensity artifacts which in some cases greatly reduces the image quality. These artifacts can be divided mainly into three cathegories.

First of them is the main magnetic field distortion. This artifacts are the results of the inhomogeneities in B_0 field. The distortions can be spatial, intensity or both.

Secondly, the problems in the gradient field coils creates the gradient field artifacts in the image. An inhomogeneity along the gradient direction or the abnormal currents passing through the coils are the underlying factors of such distortions.

Thirdly, bias field, known as RF (B_1) inhomogeneity is the presence of an undesired variation in signal intensity across an image. The cause is either a nonuniform B_1 field or a nonuniform sensitivity in a receive only coil. Some RF coils, such as surface coils, naturally have variations in sensitivity and will always cause bias field to be present in the image. The presence of this artifact in other coils may be due to the failure of an element in the RF coil or the presence of a metal object in the body [11]. Bias field is the most important signal intensity artifact in MRI as it is present in all data and significantly reduces the performance of post processing applications. Thus, we will concentrate on the reduction of this artifact in the following sections.

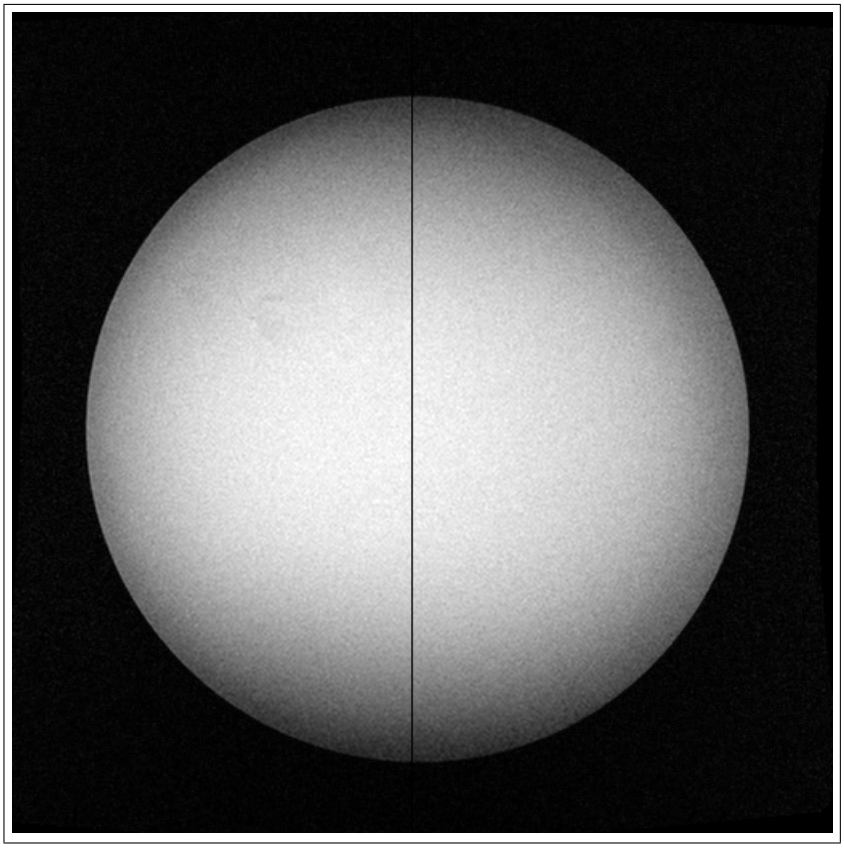

Figure 2.1 Bias Field Distortion in T_1-Weighted Phantom Scan.

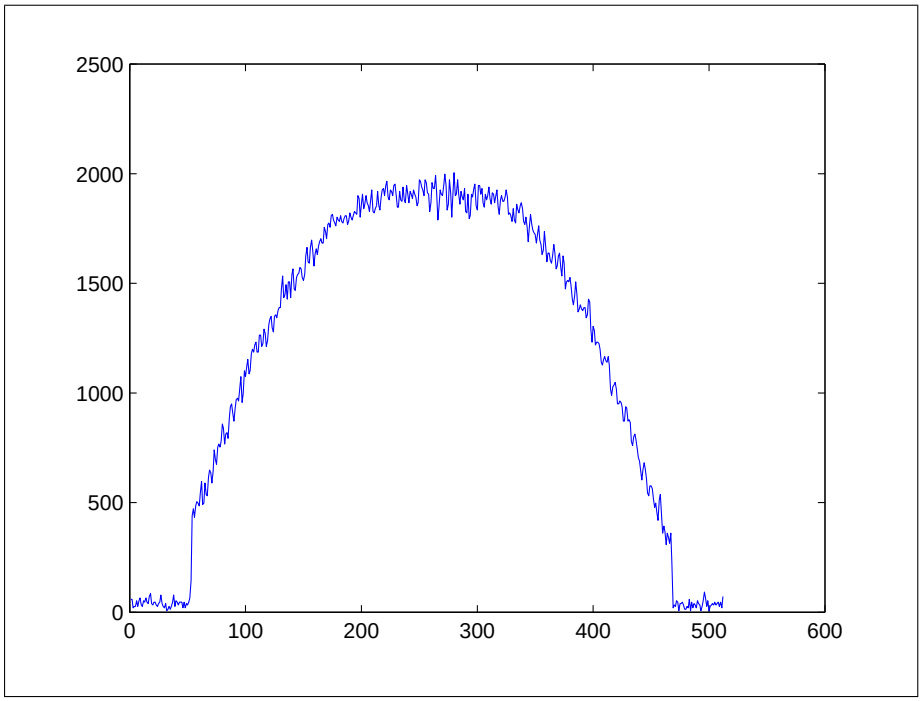

Figure 2.2 Intensity Profile.

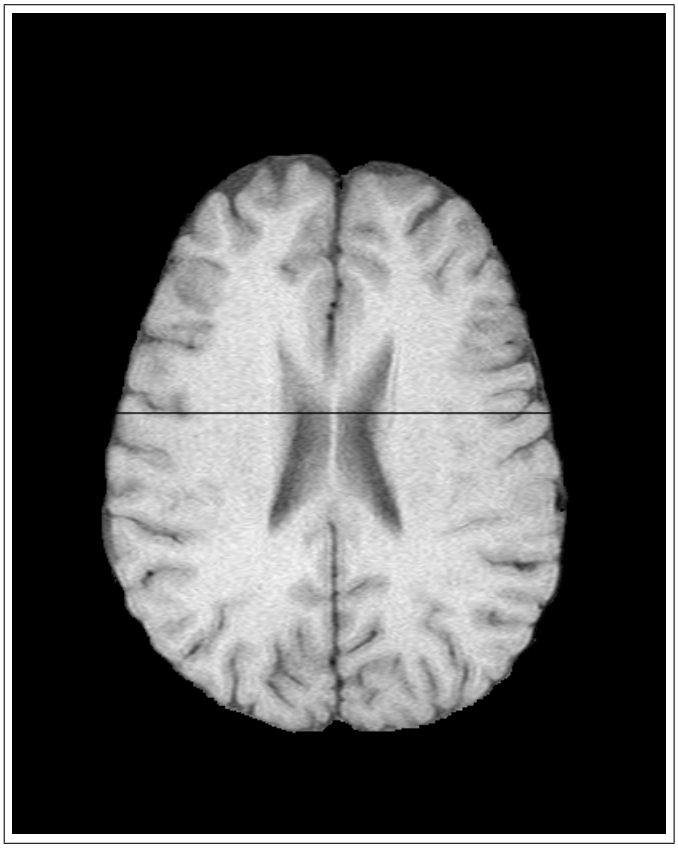

Figure 2.3 T_1-weighted MR Image.

In Figure 2.1 it is easy to visualize the effect of bias field distortion. The figure is a scan of homogeneous phantom which is a standard object used to measure the degree of distortion in the machine. The inhomogeneity in the slice is obvious. The intensity inhomogeneity can be better visualized if one plots the intensity values of the pixels in just one row or column. The intensity profile for the vertical black line in the figure can be seen in Figure 2.2. Figure 2.3 is a T_1-weighted MR head scan. The pixel intensities corresponding to the horizontal black line are plotted. The inhomogeneity in Figure 2.4 is the bias field effect on the MR data.

The most intuitive approach to intensity inhomogeneity correction is the use of high-pass filter for smoothing. This approach assumes that intensity inhomogeneity is a slowly varying, low frequency signal which can be eliminated by high pass filters. However, since the imaged objects themselves usually contain low frequencies which is obviously the case for MR brain scans, filtering methods often fail to produce mean-

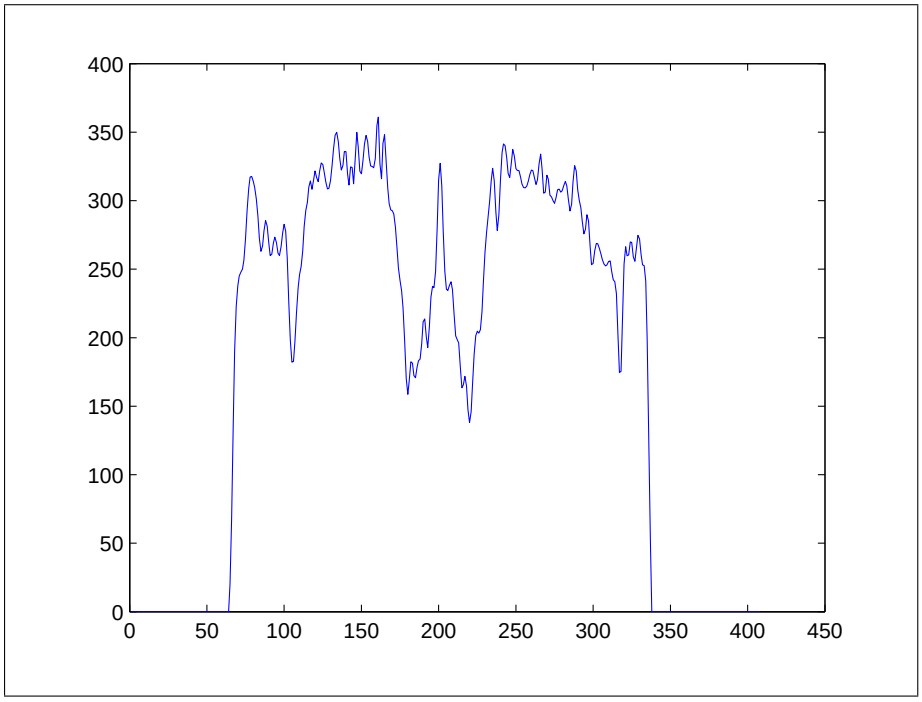

Figure 2.4 Intensity Profile.

ingful corrections. In Dawant *et al* (1993), bias field is estimated by fitting splines to the intensities at points selected on the images. This process again fails for complicated RF distributions. The information minimization technique (Likar *et al* 2001), by which the bias field is modeled by polynomials, has proved to be robust and accurate. However, if higher dynamics are present in the bias field, the order of polynomials has to be raised to 6 or more which in turn increases the number of parameters which should be optimized during the process, which makes optimization very difficult and time consuming [12]. In [12], a nonparametric method combining the intensity and spatial information is proposed. This method is proved to be accurate for even higher dynamics in the bias field but is a separate process from segmentation and depends on the selection of three different parameters used in correction. This usually requires intervention of the operator during the correction process.

2.2 ML Classification

Maximum likelihood classification is one of the most widely used techniques in segmentation problems. It is a popular statistical tool used for fitting a mathematical model to data. Its use in image segmentation is explained below.

Let $\mathcal{L}$ and $\mathcal{D}$ be two alphabets;

$$\mathcal{L} = \{1, 2, ..., l\}, \quad \mathcal{D} = \{1, 2, ..., d\}. \tag{2.1}$$

Let $\mathcal{S} = \{1, 2, ..., N\}$ be the set of indexes and $\mathcal{R} = \{r_i, i \in S\}$ denote any family of random variables indexed by $\mathcal{S}$ in which each random variable R_i takes a value r_i in its state space. Such a family r is called a random field. The joint event $(R_i = r_i, ..., R_N = r_N)$ is simplified to $R = \mathbf{r}$ where $r = \{r_1, ..., r_N\}$ is a *configuration* of R corresponding to a realization of this random field. Let X and Y be two such random fields whose state spaces are $\mathcal{L}$ and $\mathcal{D}$, respectively, so that for $\forall i \in \mathcal{S}$ we have $X_i \in \mathcal{L}$ and $Y_i \in \mathcal{D}$. Let $\mathbf{x}$ denote a configuration of X and $\mathcal{X}$ be the set of all possible configurations so that;

$$\mathcal{X} = \{\mathbf{x} = (x_1, ..., x_N) \mid x_i \in \mathcal{L}, i \in \mathcal{S}\}. \tag{2.2}$$

Similarly, let $\mathbf{y}$ be a configuration of Y and $\mathcal{Y}$ be the set of all possible configurations so that;

$$\mathcal{Y} = \{\mathbf{y} = (y_1, ..., y_N) \mid y_i \in \mathcal{D}, i \in \mathcal{S}\}. \tag{2.3}$$

Given $X_i = l$, Y_i follows a conditional distribution as;

$$p(y_i \mid l) = f(y_i; \theta_l), \quad \forall l \in \mathcal{L}, \tag{2.4}$$

where θ_l is the set of parameters. For all l, the function family $f(\cdot; \theta_l)$ has the same known analytic form.

Using Eq 2.4 with Bayes' Theorem yields;

$$p(l \mid y_i) = \frac{p(y_i \mid l)p(l)}{p(y_i)}. \tag{2.5}$$

In Eq 2.5, $p(y_i)$ is any constant in any case so, can be dropped. Moreover, although it is not the case for brain MR images, $p(l)$'s for each tissue types can be taken the same so this term can be dropped, too, resulting in;

$$p(l \mid y_i) \propto p(y_i \mid l). \tag{2.6}$$

Thus, for a given pixel intensity, ML classification estimates the class label according to the following criteria;

$$\hat{x} = arg \max_{l \in \mathcal{L}} p(y_i \mid l). \tag{2.7}$$

where $\hat{x}$ is the estimated class label corresponding to the pixel i with intensity value y_i.

In Eq 2.7 Gaussian distributions are used for almost every application. That is;

$$p(y_i \mid l) = g(y; \theta_l) = \frac{1}{\sqrt{2\pi\sigma_l^2}} exp\left(-\frac{(y-\mu_l)^2}{2\sigma_l^2}\right). \tag{2.8}$$

where $\theta_l = (\mu_l, \sigma_l)$ is the parameter set for pixel i. In the parameter set μ_l denotes the mean and σ_l denotes the standard deviation of the class l.

2.3 True-T_1 and True-T_2 Images

Recently a novel approach for the elimination of RF coil inhomogeneity artifacts is proposed that depends on true-T_1 and T_2 images instead of the weighted MR images [11]. The method relies on data acquisition at different T_E and T_R values.

2.3.1 Data Acquisition

Calculation of true-T_1 and true-T_2 values for brain tissues requires the acquisition of images at different imaging parameters.

Signal intensity in MRI for spin-echo sequence can be expressed as;

$$A_E = M_z^0 \left(1 - e^{-T_R/T_1}\right) e^{-T_E/T_2}, \tag{2.9}$$

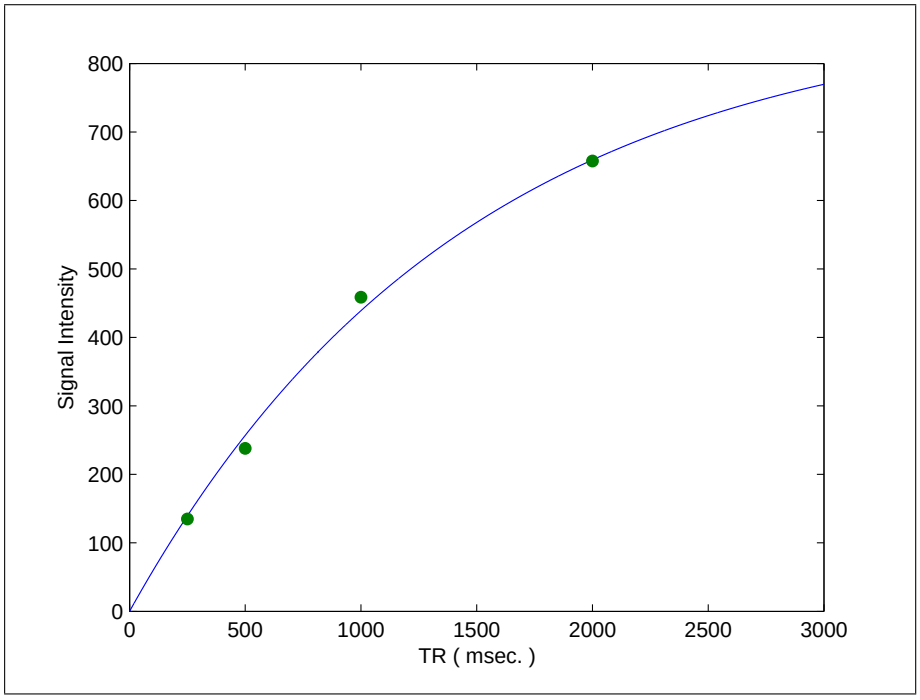

Figure 2.5 T_1 Relaxation Characteristic Curve.

where A_E is the signal intensity acquired, M_z^0 is the proton density, T_R is the repetition time and T_E is the echo time.

For the calculation of T_1 values, first of all, a short T_E relative to the T_2 values of the tissues must be selected in order to eliminate T_2 effect on the images. This kind of a image is referred to as T_1-weighted MR image.

With a short T_E duration, the signal intensity reduces to the following;

$$A_E = M_z^0 \left(1 - e^{-T_R/T_1}\right). \tag{2.10}$$

The exponentially increasing curve in Figure 2.5 can be sampled by changing T_R values.

The calculation of T_2 values follows a similar procedure. In that case, a relatively

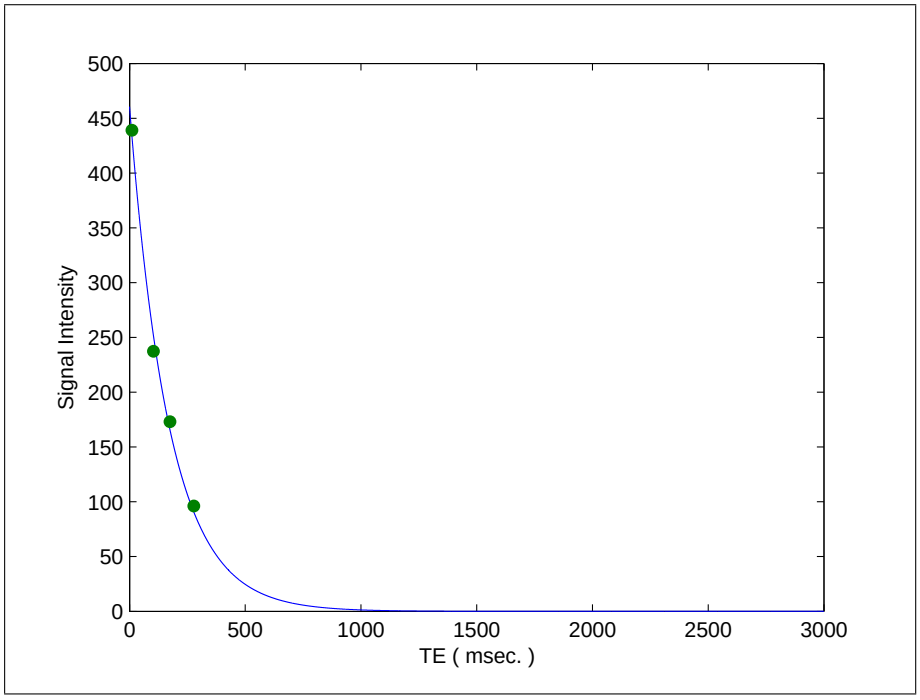

Figure 2.6 T_2 Relaxation Characteristic Curve.

long T_R relative to the T_1 values of the tissues must be used in order to eliminate T_1 effect on the images and T_E should be varied to be able to sample the decreasing exponential curve in Figure 2.6. The image gathered by this way is referred to as T_2-weighted MR image. The signal intensity A_E with T_1 effect eliminated reduces to;

$$A_E = M_z^0 e^{-T_E/T_2}. \tag{2.11}$$

2.3.2 Motion Artifacts and Registration

As the method requires the acquisition of more than one image for each slice, motion of the subject inside the MR machine becomes one of the biggest issues. Without correcting that artifact, the method becomes unreliable and useless. For a pixel to represent the same region of the tissue in the brain, head motions should be eliminated before processing the data. For that purpose, an image registration algorithm was used. Moreover, during data acquisition the stabilizers of the MR images can be used.

2.3.3 Segmentation of True Parameter Images

After finding the true-T_1 and true-T_2 images from the data collected, ML classifier can be used in order to segment brain tissues, namely WM, GM and CSF. Segmentation can be performed on just true-T_1 or true-T_2 images as well as on true-T_1 vs. true-T_2 image by constructing a multivariate Gaussian distribution. By doing so, one can use the full information coming from both the true-T_1 and true-T_2 images, resulting in a more accurate and reliable segmentation.

3. METHOD

ML classification is one of the most widely used techniques in medical image processing. Its mathematically simple model and low computational burden associated with it, makes it favorable among other techniques. However, being a pure histogram-based method forces it to just work on well defined images with low levels of noise. But it is well known that, MR data acquisition incorporates a number of factors which degrade image quality. One and probably the most important problem in MR data is the B_1 inhomogeneity artifact which, in some cases, dramatically reduces the accuracy of, especially automatic, post-processing applications.

As it is crucial to detect absolute or relative volumes of different tissues in brain for reliable diagnosis and surgical planning, the need for a more accurate and clinically usable method for medical image segmentation of brain images emerges immediately. The method in [11] addresses that problem and solves it in a great extent with high rates of success. Although being a golden standard in segmentation of brain MR images, this method brings a number of issues with it. First of all,the method is clinically unfeasible as it requires the subject to be scanned for hours which is a great problem, especially for some people who have claustrophobia. In addition, the cost of multiple scans makes the method unaffordable for almost all cases. Moreover, the time required to gather enough scans brings another problem with it, motion artifacts. These artifacts can be reduced during scan time by the use of stabilizers, but remaining motion artifacts must strictly be removed before proceeding any further, which is an additional computational burden.

To overcome the difficulties explained above, a novel approach to brain MR image segmentation is proposed in this study. MRF modeling and its application in image segmentation have been investigated by many other researchers [8, 13, 14] and in recent years has become popular. However, the application of MRF theory in brain MR image segmentation has confined to the use of only T_1 or only T_2-weighted

images. A multimodal segmentation of MR images has not been reported yet. In this work, a multimodal brain MR image segmentation using hidden Markov random field model with expectation maximization algorithm is presented. Maximum *a posteriori* estimates are adopted for the optimization and *highest confidence first* algorithm is applied for the convergence of MRFs.

3.1 MRF Theory

Markov random fields theory is a branch of probability theory for analyzing the spatial or contextual dependencies of physical phenomena which is first described in physics for lattice systems. It is used in visual labeling, especially for segmentation of the images and edge-detection algorithms [14]. The modeling of the contextual dependencies among image pixels is achieved through the encoding of mutual influences between neigboring pixels with the use of conditional distributions.

In an MRF, the sites in $\mathcal{S}$ are related to one another via a *neighborhood system*, which is defined as $\mathcal{N} = \{\mathcal{N}_i, i \in \mathcal{S}\}$, where $\mathcal{N}_i$ is the set of all sites neighboring i, $i \notin \mathcal{N}_i$ and $i \in \mathcal{N}_j \Leftrightarrow j \in \mathcal{N}_i$. A random field X is said to be an MRF on $\mathcal{S}$ with respect to a neighborhood system $\mathcal{N}$ if and only if;

$$\begin{aligned} &P(\mathbf{x}) > 0, \quad \forall \mathbf{x} \in \mathcal{X} \\ &P(x_i \mid x_{\mathcal{S}-\{i\}}) = P(x_i \mid x_{\mathcal{N}_i}). \end{aligned} \tag{3.1}$$

In many applications such as $3D$ modeling, multidimensional neighborhood systems can be created [2].

According to the Hammersley-Clifford theorem [15], an MRF can be expressed by Gibbs distribution. Thus;

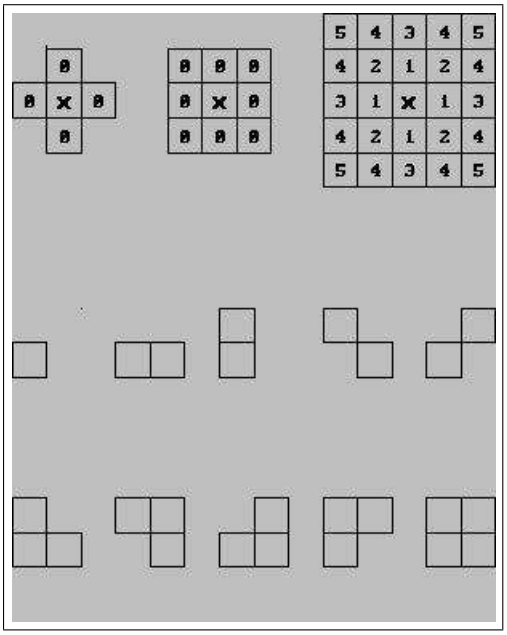

Figure 3.1 Sites and Cliques in an Image.

$$P(\mathbf{x}) = Z^{-1} exp\left(-U(\mathbf{x})\right), \tag{3.2}$$

where Z is a normalizing constant called the *partition function* and $U(\mathbf{x})$ is an *energy function* of the form;

$$U(\mathbf{x}) = \sum_{c \in \mathcal{C}} V_c(\mathbf{x}), \tag{3.3}$$

which is a sum of *clique potentials* $V_c(\mathbf{x})$ over all possible cliques $\mathcal{C}$. A *clique* c is defined as a subset of sites in $\mathcal{S}$ in which every pair of distinct sites are neighbors, except for single-site cliques. The value of $V_c(\mathbf{x})$ depends on the local configuration of clique c.

An example for sites and cliques in an image domain can be seen in Figure 3.1.

For more detail on MRF and Gibbs distribution, the reader is referred to [8].

3.1.1 HMRF Model

"The concept of a *hidden Markov random field* model is derived from *hidden Markov models* (HMM), which are defined as stochastic processes generated by a Markov chain whose state sequence cannot be observed directly, only through a sequence of observations. Each observation is assumed to be a stochastic function of the state sequence. The underlying Markov chain changes its state according to a $l \times l$ transition probability matrix, where l is the number of states.

Since original (HMM)s were designed as one-dimensional Markov chains with first-order neighborhood systems, they cannot directly be used in two-dimensional problems as image segmentation. A special case of a (HMM) in which the underlying stochastic process is a (MRF) instead of a Markov chain is considered for this purpose. This special case is referred to as *hidden Markov random field* model". Mathematically it can be characterized by the following:

- **Hidden Random Field (MRF)**

The random field $X = \{X_i, i \in \mathcal{S}\}$ is an underlying MRF assuming values in a finite state space $\mathcal{L}$ with probability distribution 3.2.

- **Observable Random Field**

$Y = \{Y_i, i \in \mathcal{S}\}$ is a random field with a finite state space $\mathcal{D}$. Given any particular configuration $\mathbf{x} \in \mathcal{X}$, every Y_i follows a known conditional probability distribution $p(y_i \mid x_i)$ of the same functional form $f(y_i; \theta_{x_i})$, where θ_{x_i} are the involved parameters. This distribution is called the *emission probability function* and Y is also referred to as the *emitted random field*.

- **Conditional Independence**

For any $\mathbf{x} \in \mathcal{X}$, the random variables Y_i are conditionally independent;

$$P(\mathbf{y} \mid \mathbf{x}) = \prod_{i \in \mathcal{S}} P(y_i \mid x_i). \tag{3.4}$$

Based on the above, the joint probability of (X, Y) can be written as;

$$P(\mathbf{y}, \mathbf{x}) = P(\mathbf{y} \mid \mathbf{x}) P(\mathbf{x}) \tag{3.5}$$

$$= P(\mathbf{x}) \prod_{i \in \mathcal{S}} P(y_i \mid x_i). \tag{3.6}$$

According to the local characteristics of MRFs, the joint probability of any pair of (X_i, Y_i), given X_i's neighborhood configuration $X_{\mathcal{N}_i}$, is;

$$P(y_i, x_i \mid x_{\mathcal{N}_i}) = P(y_i \mid x_i) P(x_i \mid x_{\mathcal{N}_i}). \tag{3.7}$$

Thus, the marginal probability distribution of Y_i dependent on the parameter set θ and $X_{\mathcal{N}_i}$ can be computed as;

$$p(y_i \mid x_{\mathcal{N}_i}, \theta) = \sum_{l \in \mathcal{L}} p(y_i, l \mid x_{\mathcal{N}_i}, \theta) \tag{3.8}$$

$$= \sum_{l \in \mathcal{L}} f(y_i; \theta_l) p(l \mid x_{\mathcal{N}_i}), \tag{3.9}$$

where $\theta = \theta_l, l \in \mathcal{L}$. This is called the *hidden Markov random field model.*

With a Gaussian emission distribution, that HMRF model can be specified as;

$$p(y_i \mid x_{\mathcal{N}_i}, \theta) = \sum_{l \in \mathcal{L}} g(y_i; \theta_l) p(l \mid x_{\mathcal{N}_i}), \tag{3.10}$$

where θ and g are defined as in 2.8. This type of HMRFs are referred to as the *Gaussian hidden Markov random field* (GHMRF) model [14].

3.2 MRF-MAP Classification

The image segmentation problem here is the assignment of a proper label taking a value from the set $\mathcal{L}$ to each image pixel. Pixels are indexed by $\mathcal{S}$ and characterized by an intensity value y_i from the set $\mathcal{D}$. A labeling of the lattice $\mathcal{S}$ is denoted by $\mathbf{x}$, where $x_i, i \in \mathcal{S}$ is the corresponding class label of pixel i. $\hat{\mathbf{x}}$ is the estimate of true but unknown labeling of $\mathcal{S}$. The problem of segmenting an image can be seen as the problem of recovering the true labeling given the observed image $\mathbf{y}$ [2].

The criterion used in the estimation of $\mathbf{x}$ is given below;

$$\hat{\mathbf{x}} = arg \max_{\mathbf{x} \in \mathcal{X}} \{P(\mathbf{y} \mid \mathbf{x}) P(\mathbf{x})\}. \tag{3.11}$$

From 3.11, the prior probability of the class and the likelihood probability of the observation need to be computed. Since $\mathbf{x}$ is considered as a realization of an MRF, its prior probability can be derived from;

$$P(\mathbf{x}) = \frac{1}{Z} exp\left(-U(\mathbf{x})\right). \tag{3.12}$$

It is also assumed that the pixel intensity y_i follows a Gaussian distribution with parameters $\theta_i = \{\mu_l, \sigma_l\}$, given the class label $x_i = l$;

$$p(y_i \mid x_i) = g(y_i; \theta_l) = \frac{1}{\sqrt{2\pi\sigma_l^2}} exp\left(-\frac{(y_i - \mu_l)^2}{2\sigma_l^2}\right). \tag{3.13}$$

Based on the conditional independence assumption of $\mathbf{y}$ 3.4, the joint likelihood

probability is;

$$P(\mathbf{y} \mid \mathbf{x}) = \prod_{i \in \mathcal{S}} p(y_i \mid x_i)$$
$$= \prod_{i \in \mathcal{S}} \left[\frac{1}{\sqrt{2\pi}} exp\left(-\frac{(y_i - \mu_{x_i})^2}{2\sigma_{x_i}^2} - \ln(\sigma_{x_i}) \right) \right], \tag{3.14}$$

which can be written as;

$$P(\mathbf{y} \mid \mathbf{x}) = \frac{1}{Z'} exp\left(-U(\mathbf{y} \mid \mathbf{x})\right), \tag{3.15}$$

with the *likelihood energy*;

$$U(\mathbf{y} \mid \mathbf{x}) = \sum_{i \in \mathcal{S}} U(y_i \mid x_i) \tag{3.16}$$
$$= \sum_{i \in \mathcal{S}} \left[\frac{(y_i - \mu_{x_i})^2}{2\sigma_{x_i}^2} + \ln(\sigma_{x_i}) \right], \tag{3.17}$$

and the constant normalization term $Z' = (2\pi)^{N/2}$. It is easy to show that;

$$\log P(\mathbf{x} \mid \mathbf{y}) \propto -U(\mathbf{x} \mid \mathbf{y}), \tag{3.18}$$

where

$$U(\mathbf{x} \mid \mathbf{y}) = U(\mathbf{y} \mid \mathbf{x}) + U(\mathbf{x}) + const, \tag{3.19}$$

is the *posterior energy*. The MAP estimation is equivalent to minimizing the posterior energy function;

$$\hat{\mathbf{x}} = arg \min_{\mathbf{x} \in \mathcal{X}} \{U(\mathbf{y} \mid \mathbf{x}) + U(\mathbf{x})\}. \tag{3.20}$$

Although mathematically simple, this type of MAP estimation clearly presents

a huge computational burden and it is infeasible for direct calculation. Therefore, optimal solutions should be computed using some iterative optimization techniques [2]. In our study, we adopted *highest confidence first algorithm* for the optimization of MAP estimation.

3.3 Model Fitting Using EM Algorithm

In the previous section, the functional form of the statistical model that will be used in the segmentation of brain MR images was derived. However, a statistical model is not complete until its parameters are determined completely. That procedure, the estimation of model parameters, is also known as *model fitting*. What to be solved in this case is the parameter set $\theta = \{\theta_l, l \in \mathcal{L}\}$. If the Gaussian emission distribution is assumed for the observable random field y, the mean and the standard deviation of the distribution of each class should be determined, namely $\theta_l = (\mu_l, \sigma_l)$.

The data set in segmentation process is incomplete since both the class label and the parameter set are unknown and they are strongly interdependent. Thus, this kind of parameter estimation is regarded as an *incomplete-data* problem. In [16], an algorithm called *the expectation maximization algorithm* was proposed for such kind of incomplete data problems. The strategy underlying the EM algorithm consists of the following: estimate the missing part as $\hat{\mathbf{x}}$, given the current θ estimate and then use it to form the complete data set $\{\hat{\mathbf{x}}, \mathbf{y}\}$; new θ can be estimated by maximizing the expectation of the complete-data log likelihood, $\mathcal{E}[\log P(\mathbf{x}, \mathbf{y} \mid \theta)]$. Description of the EM algorithm is as follows [17]:

- *Start*

An initial estimate $\theta^{(0)}$ is decided according to Otsu thresholding.

- *The E-Step*

$$Q\left(\theta \mid \theta^{(t)}\right) = \mathcal{E}\left[\log P(\mathbf{x}, \mathbf{y} \mid \theta) \middle| \mathbf{y}, \theta^{(t)}\right]$$
$$= \sum_{\mathbf{x} \in \mathcal{X}} p(\mathbf{x} \mid \mathbf{y}, \theta^{(t)}) \log p(\mathbf{x}, \mathbf{y} \mid \theta). \tag{3.21}$$

- *The M-Step*

Maximize $Q(\theta \mid \theta^{(t)})$ to obtain next estimate;

$$\theta^{(t+1)} = arg \max_{\theta} Q(\theta \mid \theta^{(t)}). \tag{3.22}$$

Using Eq 3.10, the Q-function can be formulated as;

$$Q = \sum_{i \in \mathcal{S}} \sum_{l \in \mathcal{L}} \left\{ P^{(t)}(l \mid y_i) W + C \right\}, \tag{3.23}$$

where;

$$W = \log p^{(t)}(l \mid \mathbf{x}_{\mathcal{N}_i}) - \ln \sigma_l - \frac{(y_i - \mu_l)^2}{2\sigma_l^2}, \tag{3.24}$$

and $C = -0.5 \ln(2\pi)$.

Application of the EM algorithm yields the following update rules for the parameters;

$$\mu_l^{(t+1)} = \frac{\sum_{i \in \mathcal{S}} P^{(t)}(l \mid y_i) y_i}{\sum_{i \in \mathcal{S}} P^{(t)}(l \mid y_i)}, \tag{3.25}$$

$$\left(\sigma_l^{(t+1)}\right)^2 = \frac{\sum_{i \in \mathcal{S}} P^{(t)}(l \mid y_i)(y_i - \mu_l)^2}{\sum_{i \in \mathcal{S}} P^{(t)}(l \mid y_i)}, \tag{3.26}$$

where;

$$P^{(t)}(l \mid y_i) = \frac{g^{(t)}(y_i; \theta_l) P^{(t)}(l \mid x_{\mathcal{N}_i})}{p(y_i)}. \tag{3.27}$$

3.4 Highest Confidence First Algorithm

Highest Confidence First (HCF) is a serial, deterministic algorithm used for the convergence of MRFs where the label set is discrete, $\mathcal{L} = \{1, 2, ..., l\}$. At the beginning of the algorithm the discrete label set $\mathcal{L}$ is augmented by the inclusion of a special uncommitted label 0 as $\mathcal{L}^+ = \{\mathbf{0}, 1, 2, ..., l\}$. A label x_i is said to be *uncommitted* if $x_i = 0$, or *committed* if $x_i \in \mathcal{L}$. Initially all labels are set to 0 and the following rule is imposed for the labeling: once a site is committed, it's label cannot go back uncommitted but can change to another value in $\mathcal{L}$.

The conditional posterior potential for site i can be given as follows;

$$\begin{aligned} E_i(x_i) &= V(x_i \mid y_i, x_{\mathcal{N}_i}) \\ &= V(y_i \mid x_i) + \sum_{c:i \in c} V_c(x_i \mid x_{\mathcal{N}_i}), \end{aligned} \tag{3.28}$$

where $c : i \in c$ means any clique containing site i. After augmenting the label set the conditional potential for a committed label $x_i \in \mathcal{L}$ is defined as;

$$\begin{aligned} E_i(x_i) &= V(x_i \mid y_i, x_{\mathcal{N}_i}) \\ &= V(y_i \mid x_i) + \sum_{c:i \in c} V'_c(x_i \mid x_{\mathcal{N}_i}), \end{aligned} \tag{3.29}$$

where;

$$V'_c = \begin{cases} 0 & \text{if} \quad x_j = 0 \quad \exists j \in c; \\ V_c & \text{otherwise.} \end{cases}$$

From Eq. 3.29 one can conclude that, a site has no effect on its neighbors when it is uncommitted. In addition, when no neighbor is active, the local energy measure reduces to the likelihood of the label.

The stability of site i with respect to x is defined as

$$S_i(x) = \begin{cases} -min_{l\in\mathcal{L},l\neq l_{min}}\left[E_i(l) - E_i(l_{min})\right] & \text{if} \quad x_i = 0; \\ min_{l\in\mathcal{L},l\neq x_i}\left[E_i(l) - E_i(x_i)\right] & \text{otherwise.} \end{cases}$$

where $l_{min} = arg\min_{l\in\mathcal{L}} E_i(l)$. The stability S of an uncommitted site is the negative difference between the lowest and the second lowest local energies (conditional potentials). The stability S of a committed site is the difference between the current local energy and the lowest possible energy due to any other label. A negative stability reflects the possible change of the current label. May the following rule is imposed for deciding the order of update: At each step, only the least stable site (lowest magnitude) is allowed to change its label or to make its commitment. Suppose that $k = arg\max_i |S_i(x)|$ is the least stable site. Then if $x_k = 0$, change x_k to;

$$x'_k = arg\min_{l\in\mathcal{L}} E_k(l), \tag{3.30}$$

otherwise change x_k to;

$$x'_k = arg\min_{l\in\mathcal{L},l\neq x_k}\left[E_k(l) - E_k(x_k)\right]. \tag{3.31}$$

As opposed to the use of *iterated conditional modes* (ICM) in most applications, in this study HCF algorithm is preferred as it is reported to be better in terms of remaining energy in the image. Moreover, initialization is not a problem for HCF as it is always set to 0's at the beginning [14].

3.5 Step-by-Step HMRF-EM Algorithm

The theory underlying the segmentation of brain MR images was given in the sections above. Here the steps which cover the HMRF model with EM algorithm will be summarized.

1. Perform the initial parameter estimation for the probability distribution Eq 3.13;

2. Calculate the likelihood distribution according to;

$$p^{(t)}(y_i \mid x_i) = g^{(t)}(y_i; \theta(x_i)); \tag{3.32}$$

3. Estimate the class labels by HMRF-MAP estimation as;

$$\mathbf{x}^{(t)} = arg \max_{\mathbf{x} \in \mathcal{X}} \{P(\mathbf{y} \mid \mathbf{x}, \theta^{(t)}) + P(\mathbf{x})\}; \tag{3.33}$$

4. Calculate the posterior distribution according to;

$$P^{(t)}(l \mid y_i) = \frac{g^{(t)}(y_i; \theta_l) p^{(t)}(l \mid x_{\mathcal{N}_i})}{p(y_i)}; \tag{3.34}$$

5. Update parameters by;

$$\mu_l^{(t+1)} = \frac{\sum_{i \in \mathcal{S}} P^{(t)}(l \mid y_i) y_i}{\sum_{i \in \mathcal{S}} P^{(t)}(l \mid y_i)}, \tag{3.35}$$

$$\left(\sigma_l^{(t+1)}\right)^2 = \frac{\sum_{i \in \mathcal{S}} P^{(t)}(l \mid y_i)(y_i - \mu_l)^2}{\sum_{i \in \mathcal{S}} P^{(t)}(l \mid y_i)}; \tag{3.36}$$

6. Increment the index t by 1 and repeat from (2) until enough iterations have been performed.

For the first step above, initial parameter estimation is done using a variate of *Otsu's Algorithm* [18], namely *modified Otsu* [19].

For the Gaussian prior, in *1D*-classification Eq 3.13 is used. In *2D*-classification a multivariate version of Gaussian distribution will be used as follows;

$$p(\vec{y}_i \mid x_i) = \frac{1}{2\pi |\Sigma_{x_i}|^{1/2}} exp\left(-\frac{1}{2}(\vec{y}_i - \vec{\mu}_{x_i})^T \Sigma_{x_i}^{-1} (\vec{y}_i - \vec{\mu}_{x_i})\right). \tag{3.37}$$

where, $\vec{y}_i = [y_{T_1}, y_{T_2}]$ is the intensity vector for pixel i, $\vec{\mu}_{x_i} = [\mu_{T_1}, \mu_{T_2}]$ is the mean of intensities for class label $x_i \in \mathcal{L}$ and Σ_{x_i} is the covariance matrix for tissue

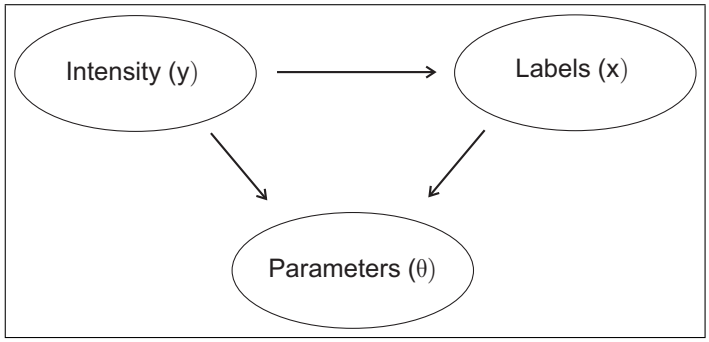

Figure 3.2 Bayesian graph of the variables.

class x_i.

In Figure 3.2, the dependencies among the variables of the segmentation problem can be better visualized.

4. RESULTS

The main goal of the proposed study was to develop a multimodal segmentation scheme which offers comparable result to the segmentation done by the use of calculated True-T_1 and True-T_2 images while greatly reducing the time required to capture data. This is done by gathering just two images, one T_1-weighted and one T_2-weighted, instead of a total of eight images required for the calculation of true parameter and using post-processing techniques on these two. To be more specific, HMRF models are used to aid segmentation which takes the information hidden in the neighborhood configurations of tissues into consideration. Moreover, using two-dimensional data, the proposed method is expected to yield better results than 1D case as the information coming from T_2 images are not linearly dependent to the information coming from T_1 images. The images used in this study were captured for the following parameters:

- T_1-weighted : $T_E = 15$ ms ; $T_R = 250, 500, 1000$ and 2000 ms.
- T_2-weighted : $T_R = 3000$ ms ; $T_E = 10, 103, 175$ and 278 ms.

These parameters are the ones which result in the best fits to the characteristic relaxation curves. Originally, a total of twelve images were taken both for T_1 and T_2-weighted images. After the comparison of the true parameters which were calculated with different combination of the images, the parameters above were chosen to be the best sampling points.

4.1 Analysis of True Parameter Images

In this part of the study, a total of eight images were used in order to construct $True - T_1$ and $True - T_2$ images according to Eq 2.10 and Eq 2.11. The classification scheme is ML estimation according to Eq 3.37. Considering the multivariate segmentation method as golden standard, $1D$ ML classification of the true parameter images

will be compared to $2D$ case. The image set used for that purpose is given below. The images used in the study are taken for the given T_E and T_R values in previous section.

All images below were used to construct true parameters image set. ML estimate is used in that part as it was proven to give segmentation results with a success of around 97% in classification of the three main tissues, namely CSF, GM and WM [11].

Calculated $True - T_1$ and $True - T_2$ images can be seen in Figure 4.9 and 4.10.

Using the ML estimation with the parameters specified in [11] yields the segmented image in Figure 4.11.

In Figure 4.11, blue parts corresponds to CSF while yellows and claret-red indicates GM and WM respectively.

For the analysis of true parameter images, $1D$ segmentations of $True - T_1$ and $True - T_2$ images were also obtained, again using ML classification.

As can be seen from Figure 4.12, the result is satisfactory considering the GM and WM discrimination however, it is poor in the sense that CSF parts of the brain could not be segmented well. On the contrary, Figure 4.13 is capable of classifying CSF better than $True - T_1$ image could. Together, these two images achieve the final goal of an accurate segmentation. Confusion matrices corresponding to the segmentation of $True - T_1$ and $True - T_2$ images are obtained by taking the $2D$ segmentation result as a reference for a better quantitative analysis.

From Table 4.1, one can conclude that most of the CSF is misclassified if $True - T_1$ images are used only.

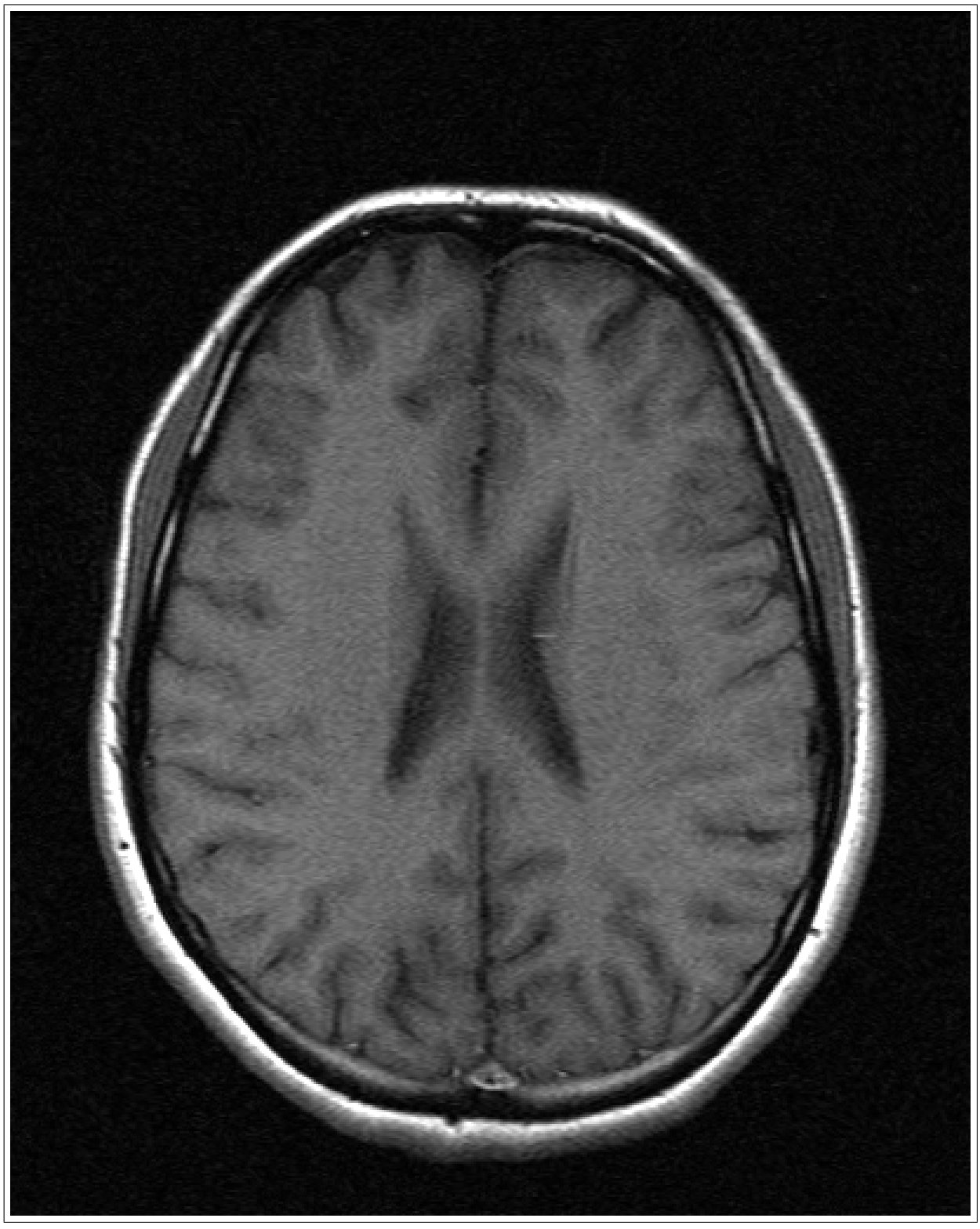

Figure 4.1 Image data ($T_E = 15\text{ms}$ $T_R = 250\text{ms}$).

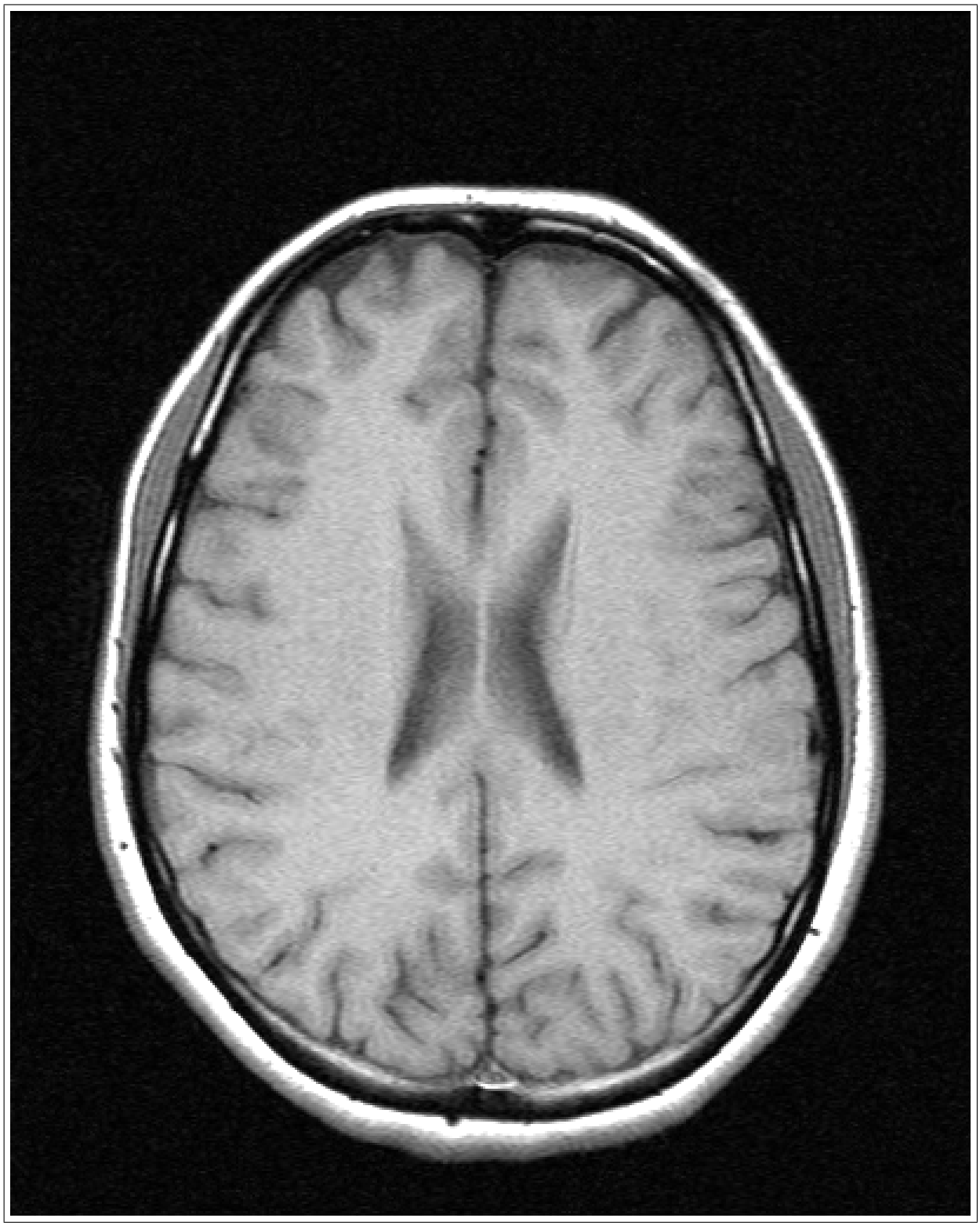

Figure 4.2 Image data ($T_E = 15\text{ms}$ $T_R = 500\text{ms}$).

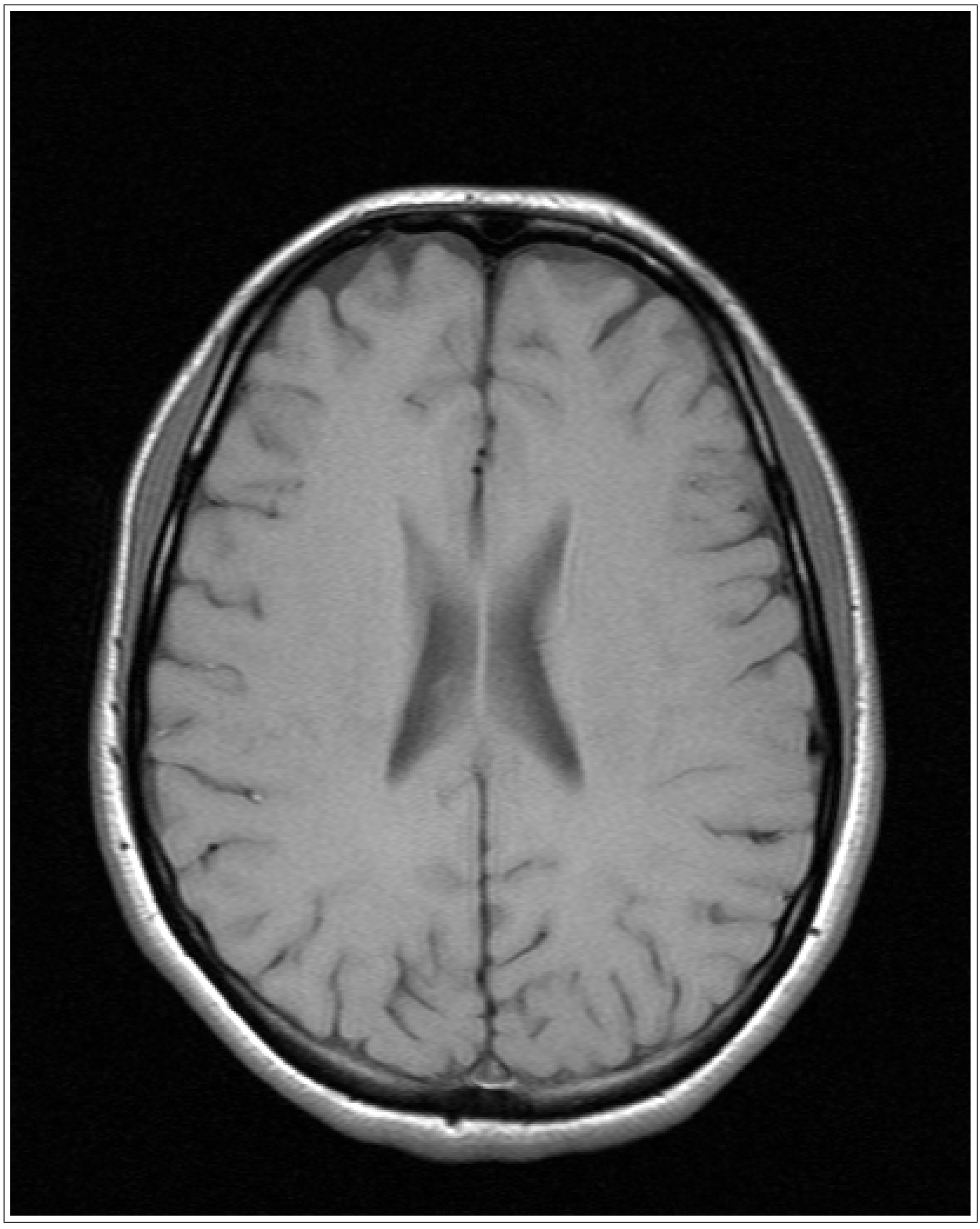

Figure 4.3 Image data ($T_E = 15\text{ms}$ $T_R = 1000\text{ms}$).

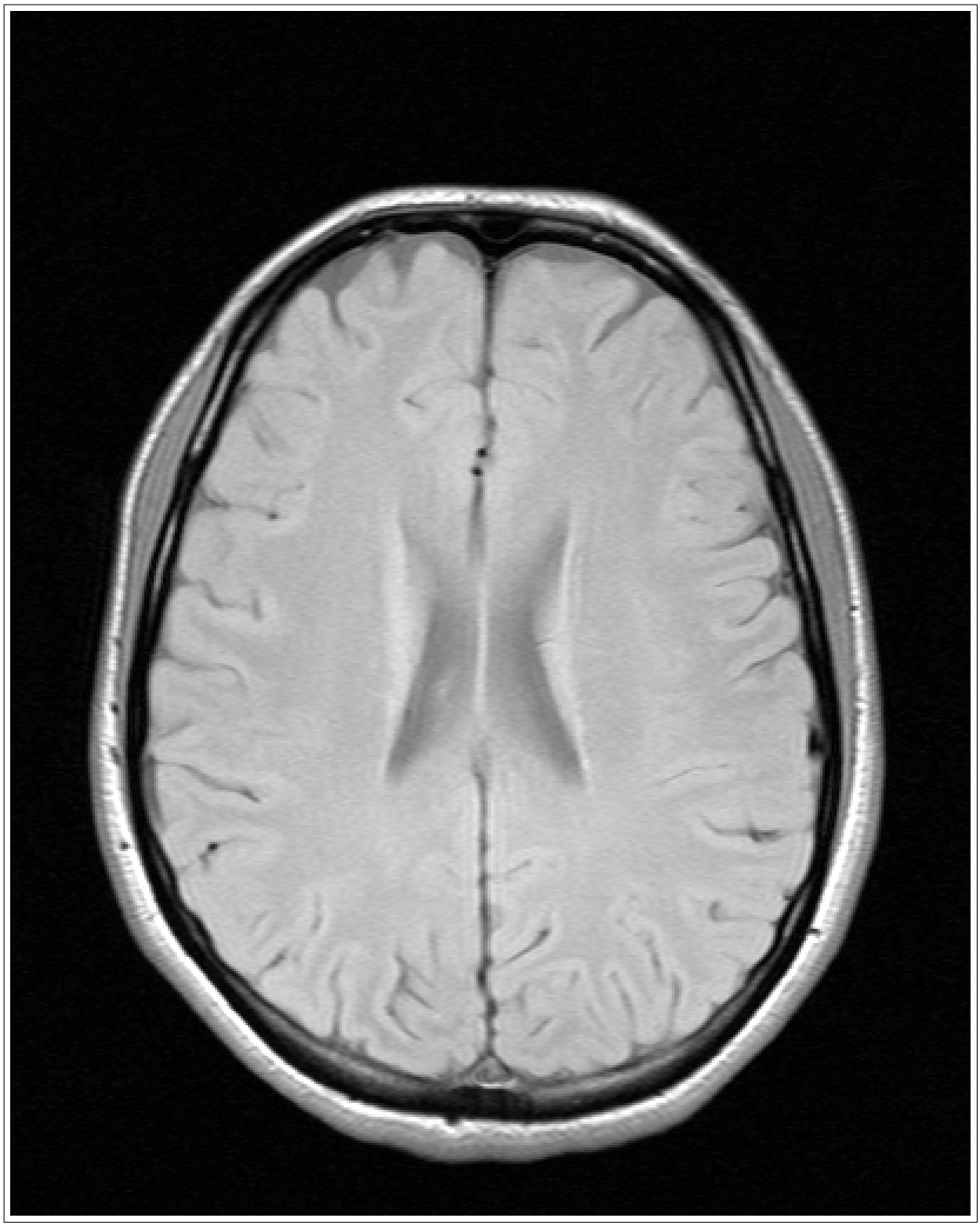

Figure 4.4 Image data ($T_E = 15\text{ms}$ $T_R = 2000\text{ms}$).

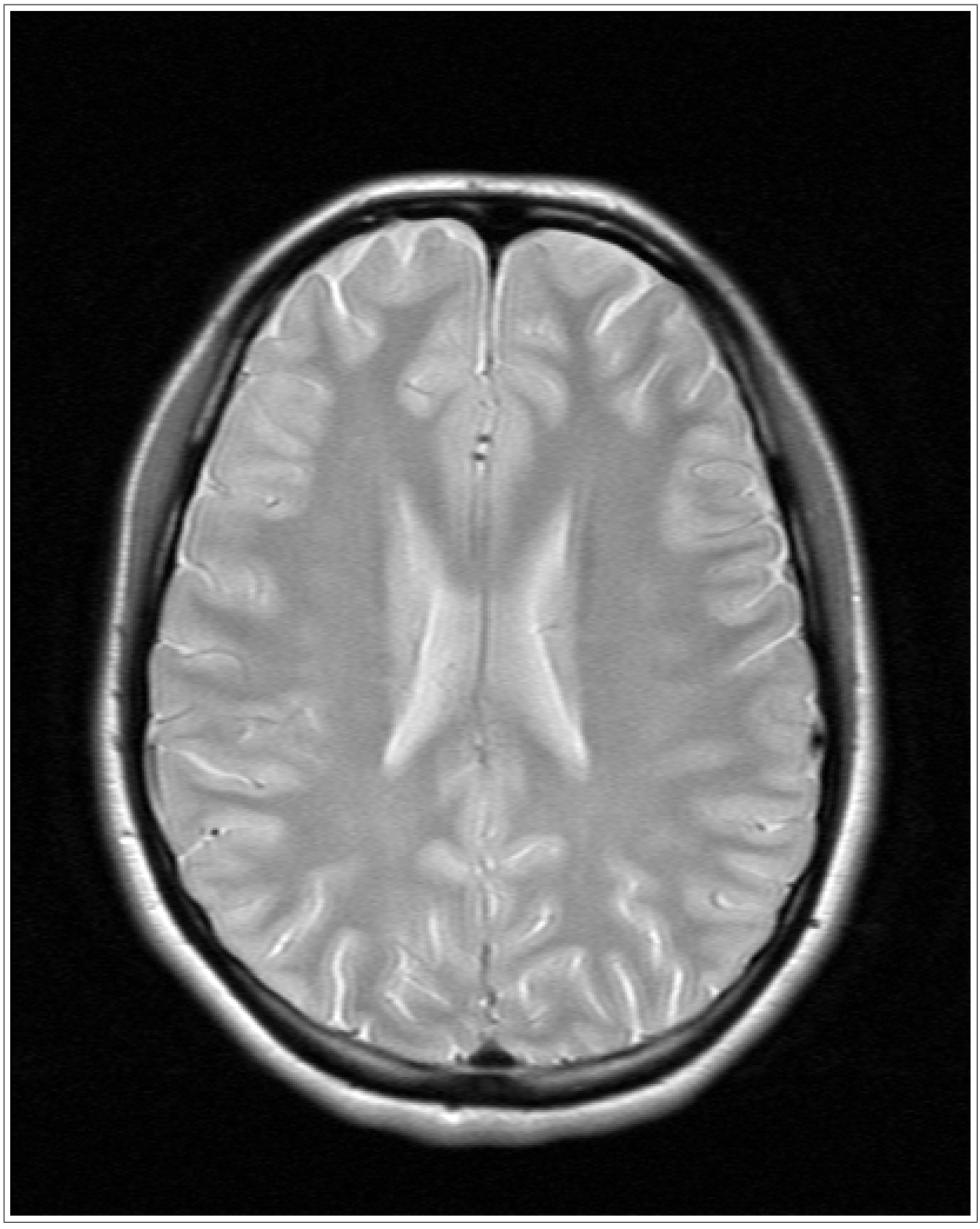

Figure 4.5 Image data ($T_R = 3000\text{ms}$ $T_E = 10\text{ms}$).

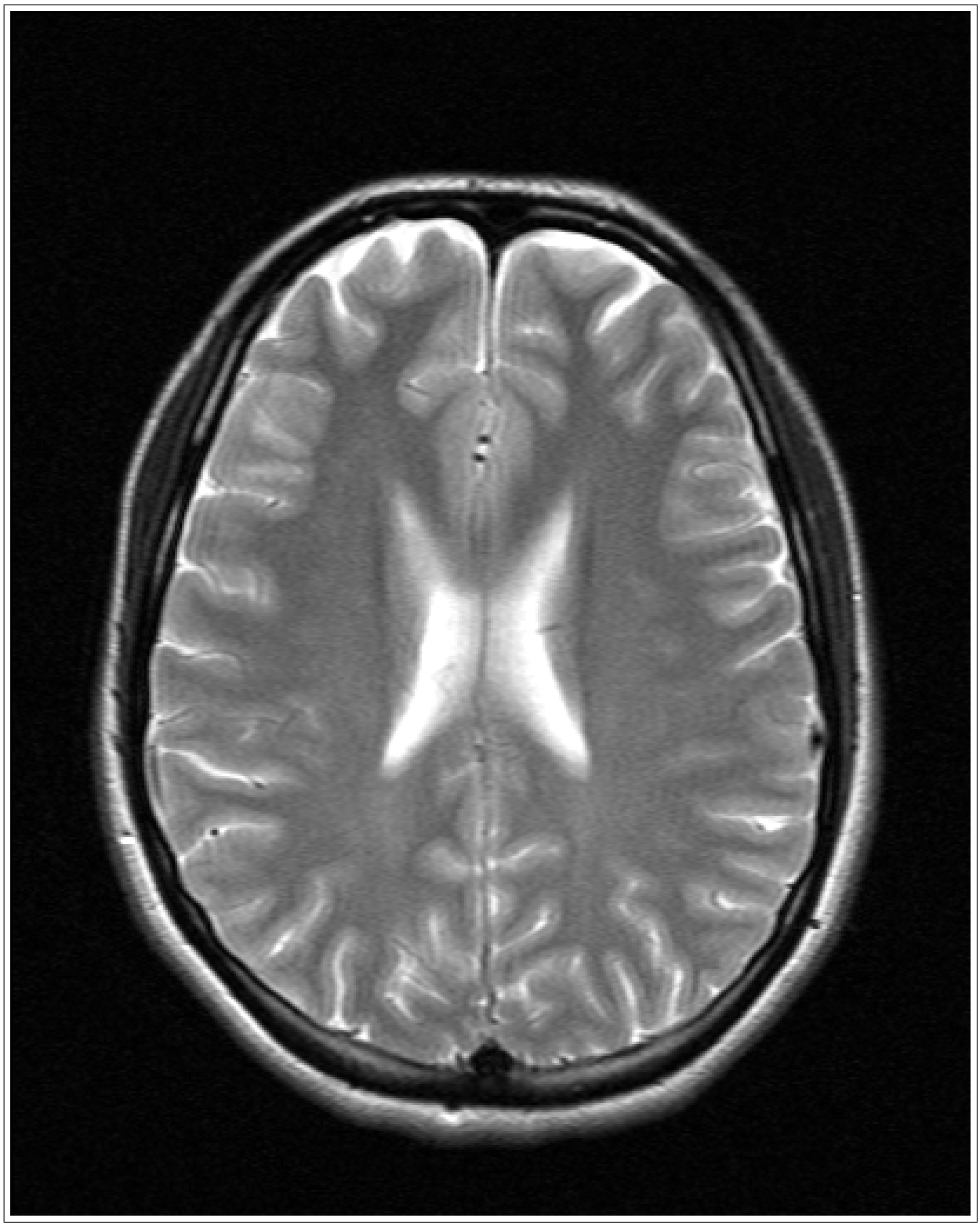

Figure 4.6 Image data ($T_R = 3000\text{ms}$ $T_E = 103\text{ms}$).

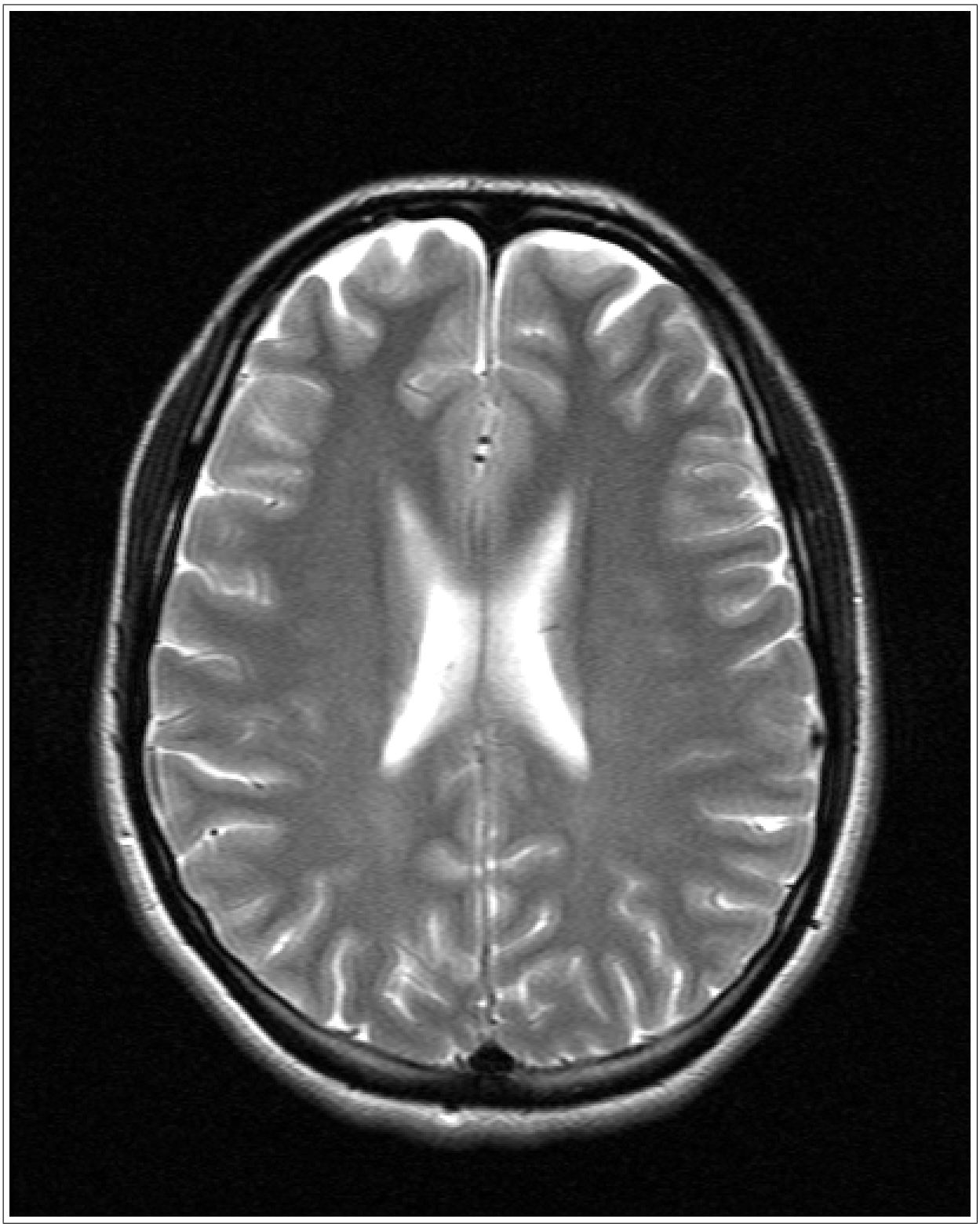

Figure 4.7 Image data ($T_R = 3000\text{ms}$ $T_E = 175\text{ms}$).

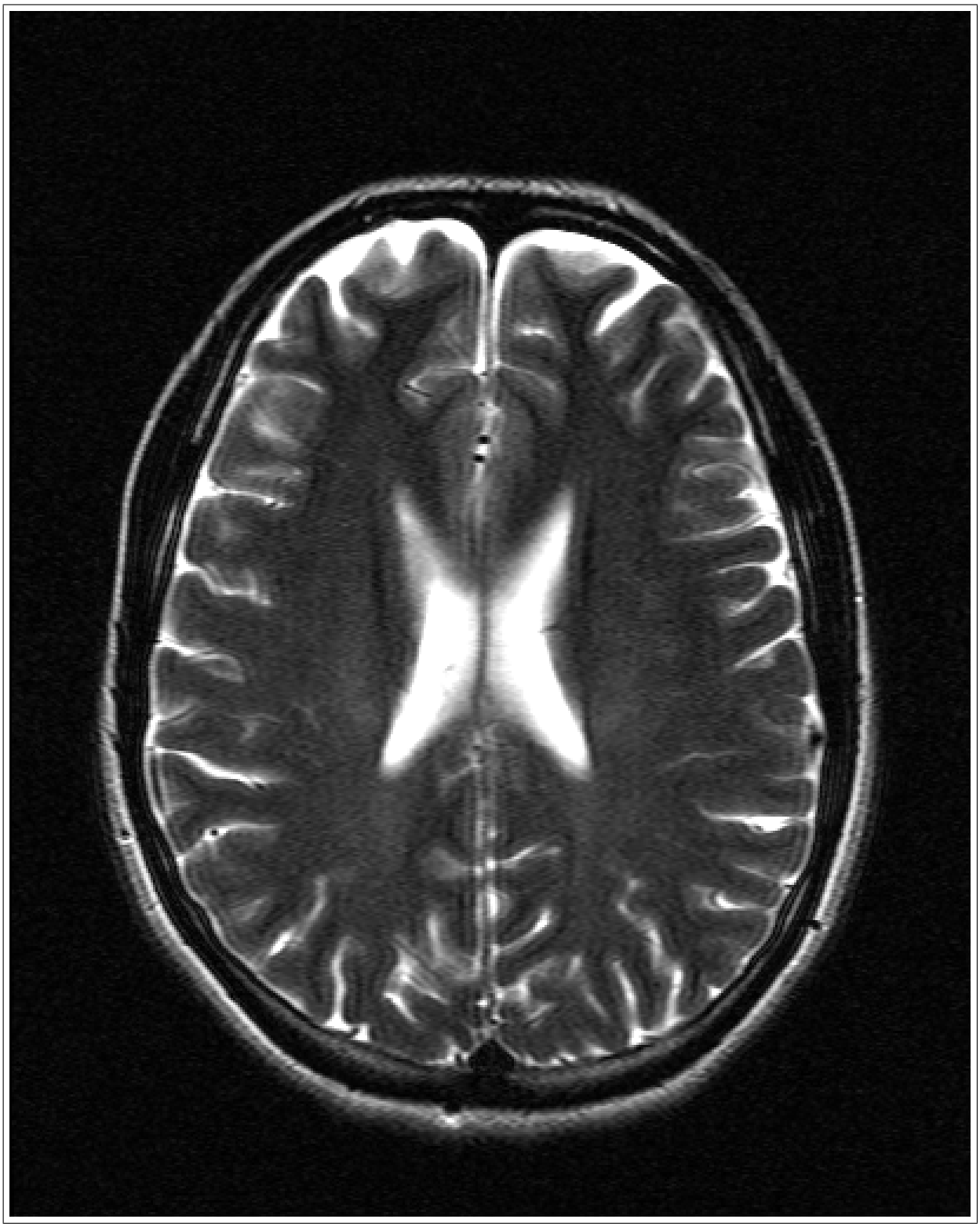

Figure 4.8 Image data ($T_R = 3000\text{ms}$ $T_E = 278\text{ms}$).

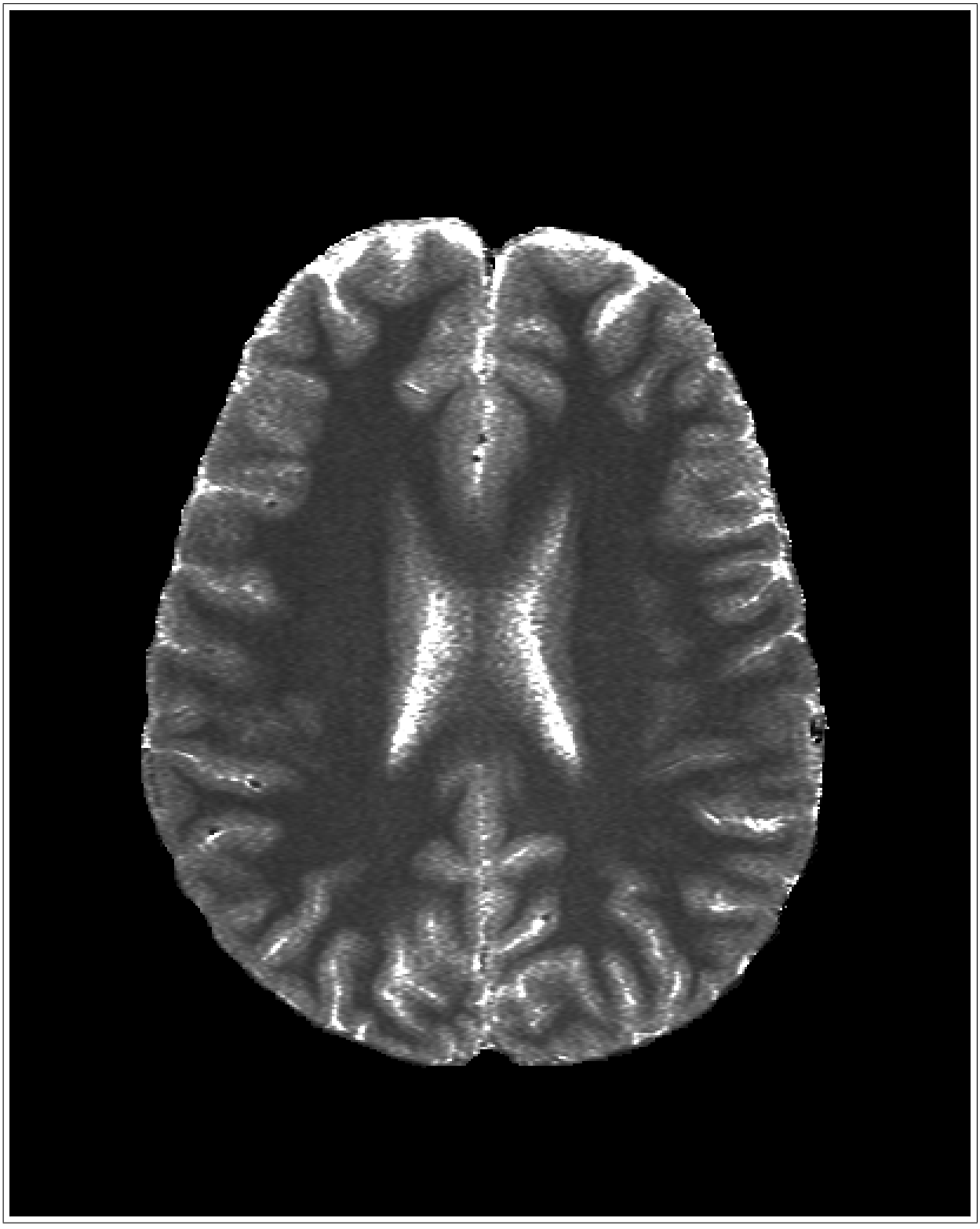

Figure 4.9 $True - T_1$ image.

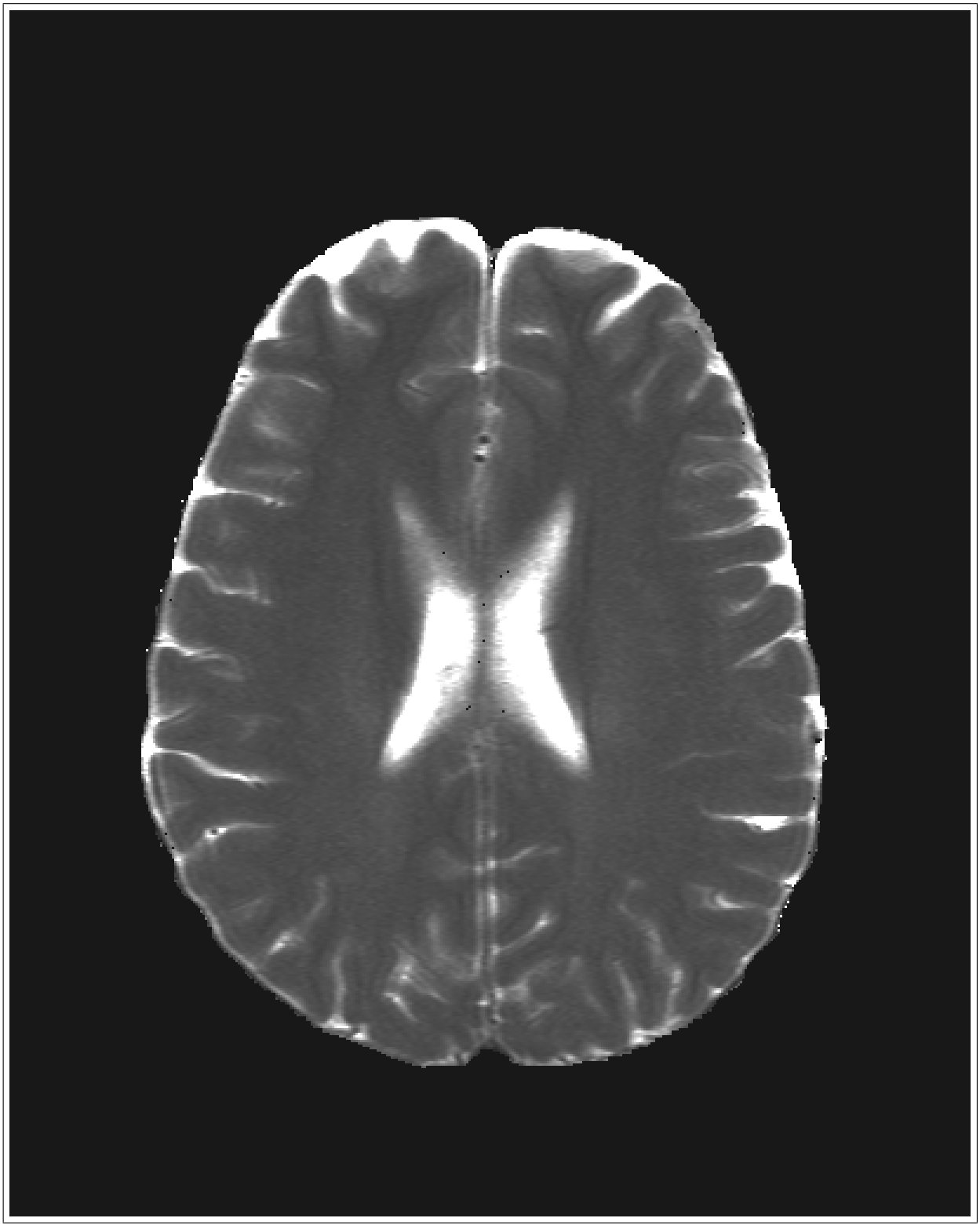

Figure 4.10 $True - T_2$ image.

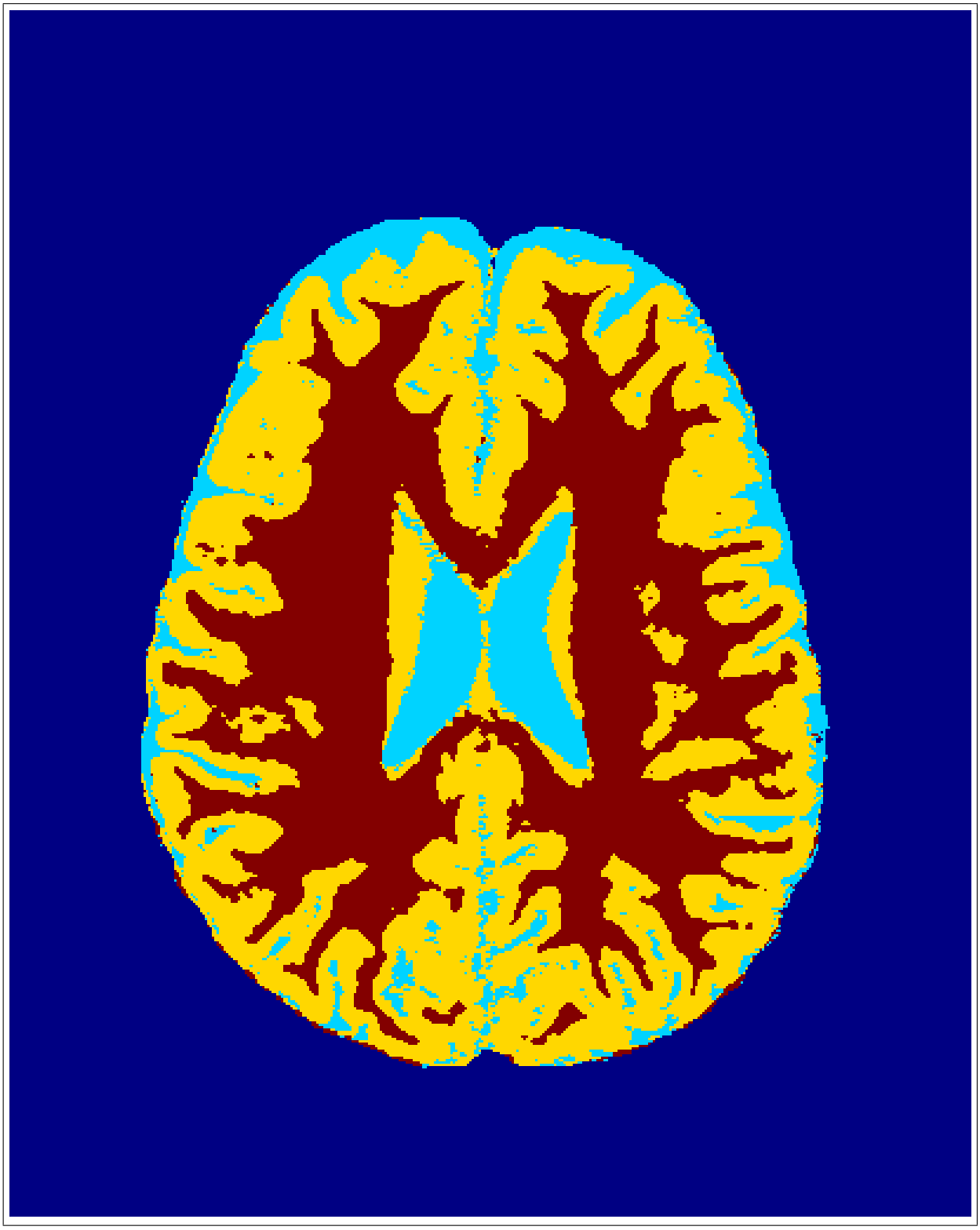

Figure 4.11 $2D$ Segmentation of the complete image set.

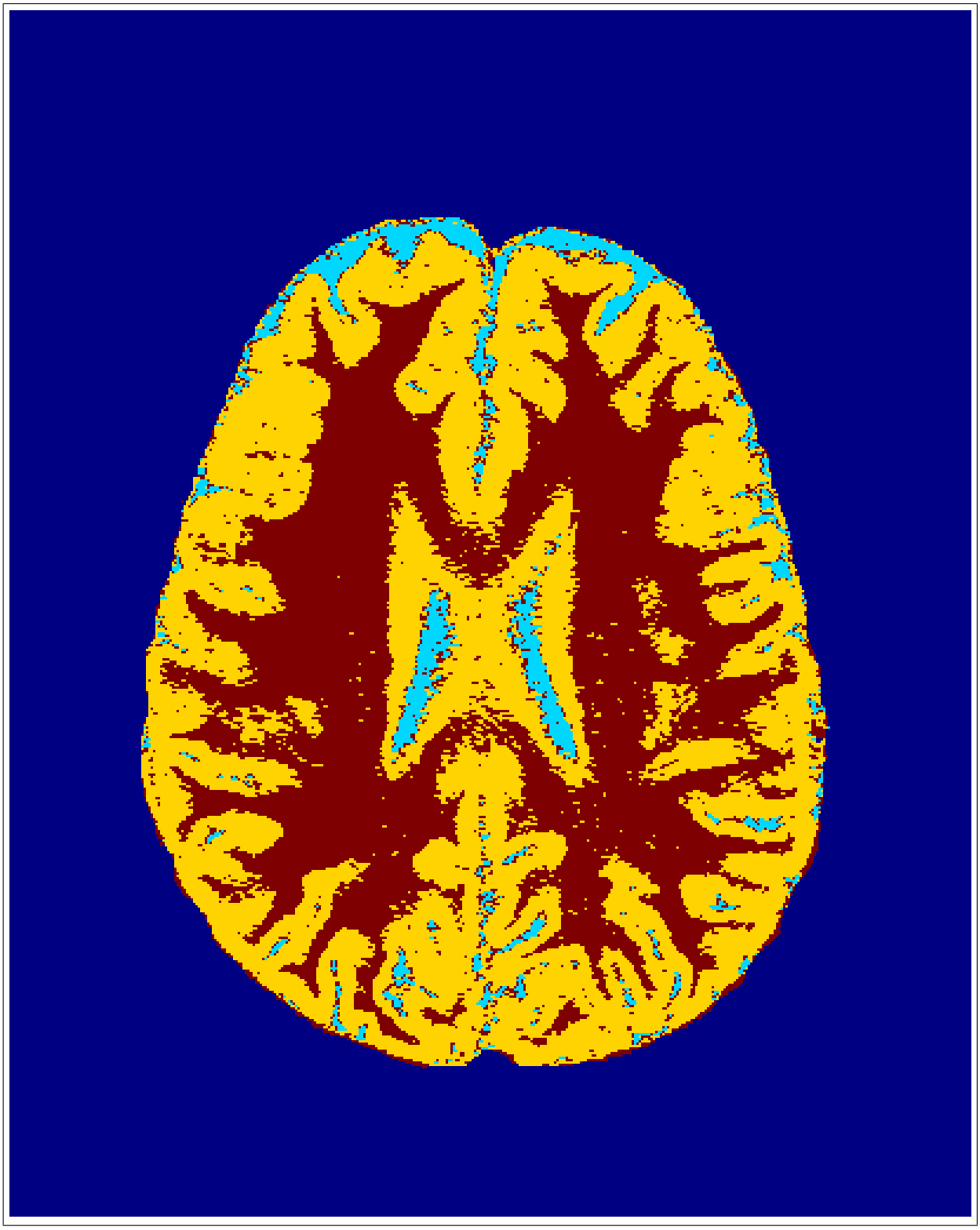

Figure 4.12 Segmented $True - T_1$ image.

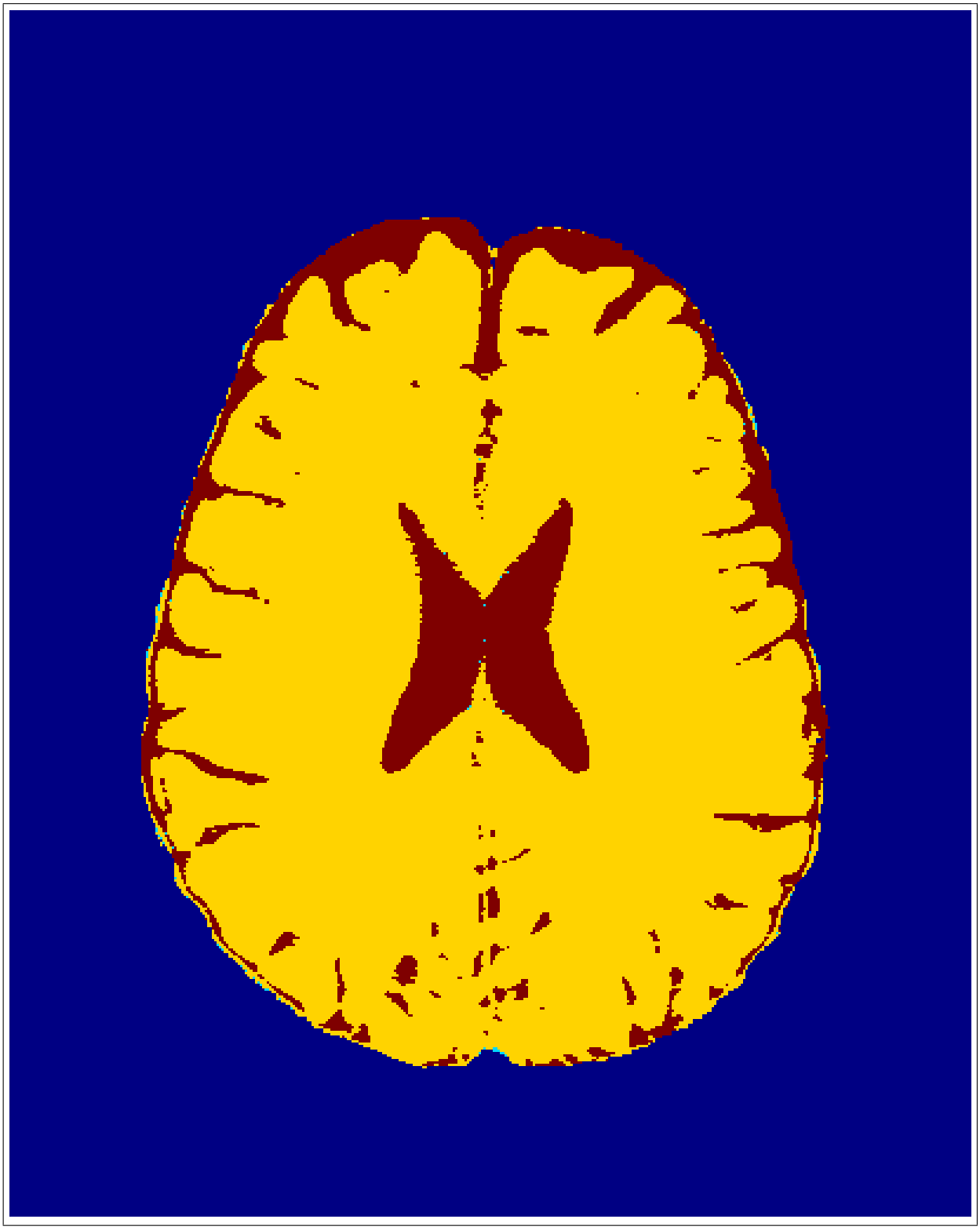

Figure 4.13 Segmented $True - T_2$ image.

Table 4.1
$True - T_1$ confusion matrix.

	CSF	GM	WM
CSF	35.98	42.85	21.17
GM	0	96.62	3.38
WM	0	3.09	96.91

Table 4.2
$True - T_2$ confusion matrix.

	CSF	GM	WM
CSF	89.92	0	10.07
GM	7.92	0	92.08
WM	0.14	0	99.86

The probability distribution of the class labels for $True - T_2$ image is given in Figure 4.14. The misclassification of GM parts as WM is the result of the closeness of the distributions corresponding to these labels.

As it is obvious from Table 4.2, main contribution of the use of $True - T_2$ images in segmentation is the capability of these images to classify CSF.

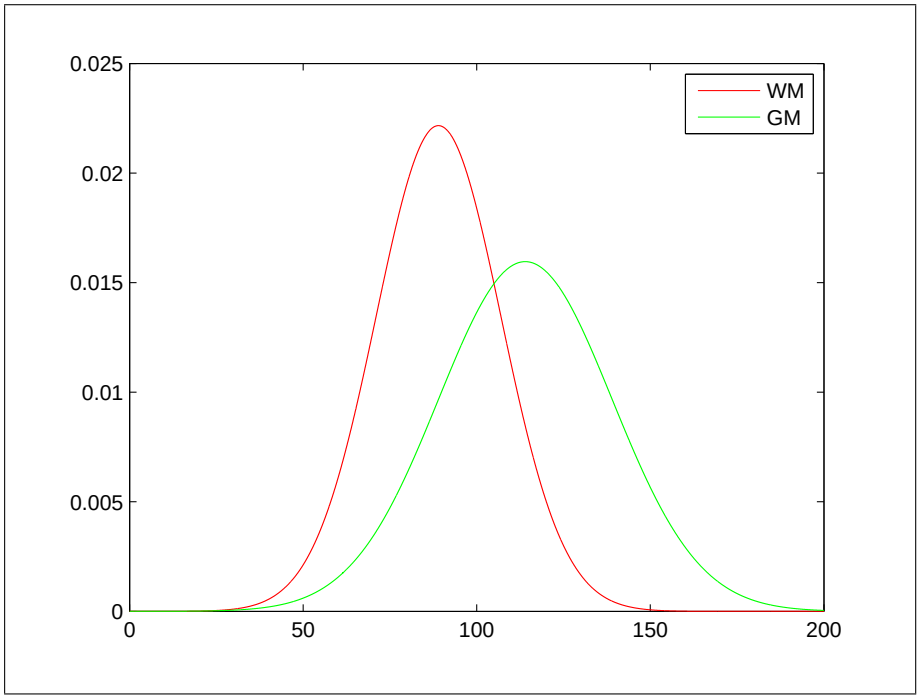

Figure 4.14 Probability distribution of WM and GM for $True - T_2$ image.

4.2 $1D$ Segmentation

In this part, individual MR data will be segmented using Otsu thresholding, ML classification and HMRF model based segmentation techniques separately.

4.2.1 Otsu Thresholding

In its basic form, Otsu's method is an image thresholding algorithm used in reduction of a gray level image to a binary image. It gives the optimum threshold separating those two classes so that their intra-class variance is minimal. However for the segmentation of brain MR images, three different classes are required in order to represent three different tissue classes. Thus, a modified version of Otsu's method is used for that purpose. In addition to being a separate segmentation technique, the parameters obtained from this algorithm are used for both ML estimation and HMRF models. The algorithm and its proof can be found in Appendix B.

Figure 4.15 is the segmentation result of Figure 4.1 using modified Otsu with three labels. The confusion matrix corresponding to this application can be seen in Table 4.3. As can be seen from the corresponding confusion matrix, the result for WM segmentation with Otsu thresholding is satisfactory while it is not the case for GM and CSF results.

Table 4.3
T_1 image confusion matrix for Otsu thresholding.

	CSF	GM	WM
CSF	71.99	26.78	1.23
GM	6.85	65.08	28.34
WM	0.86	5.14	94.00

Figure 4.16 is the segmented T_2 image. Its confusion matrix can be seen in Table 4.4.

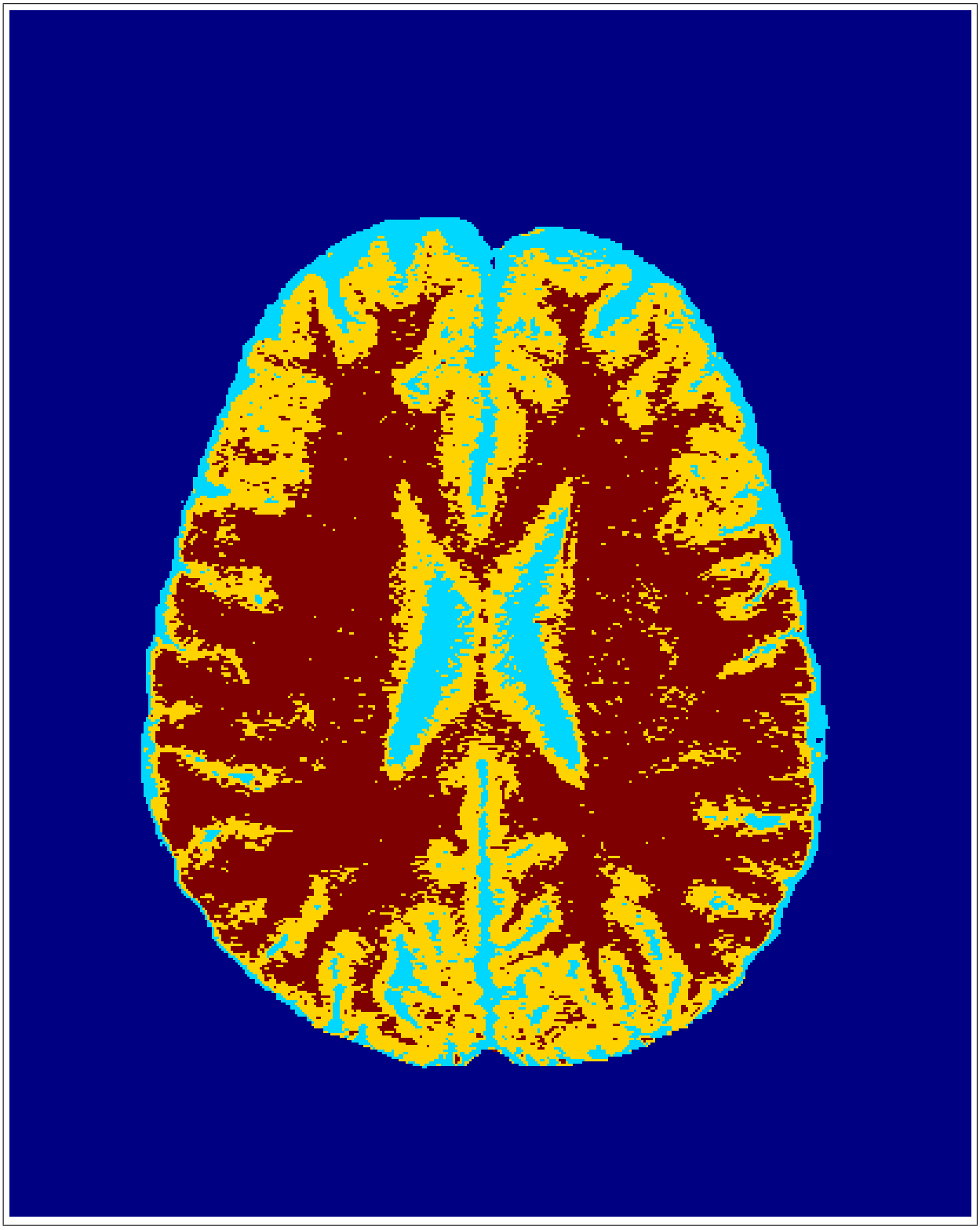

Figure 4.15 Segmented T_1 image with Otsu thresholding.

Table 4.4
T_2 image confusion matrix for Otsu thresholding.

	CSF	GM	WM
CSF	59.70	30.83	9.46
GM	1.22	67.00	31.78
WM	0	3.35	96.64

Comparing Table 4.3 and 4.4, it can be concluded that the pixel intensities in T_1 images for CSF volumes are better separated than the intensities in T_2 images does. On the other hand, segmentation results for WM and GM when T_2 images are used are better with Otsu's algorithm. As it is mentioned before, Otsu's method will be used for both ML classification and HMRF segmentation in order to find initial tissue class parameters. To be more specific, means and variances of three tissue types are calculated using that method which can be considered as a model fitting, fitting of the image histogram to the optimum Gaussian mixture.

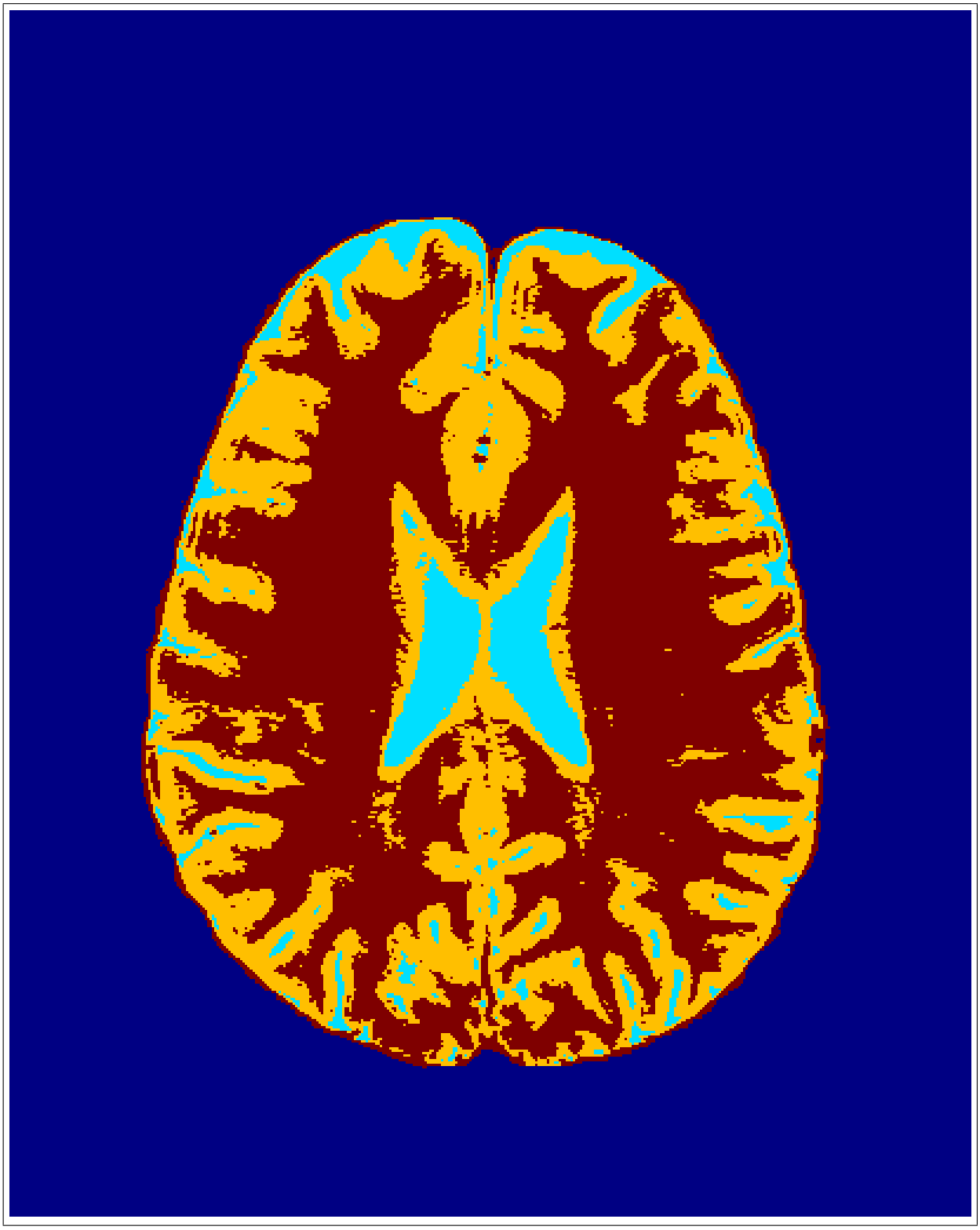

Figure 4.16 Segmented T_2 image with Otsu thresholding.

4.2.2 ML Classification

ML classification is one of the most preferable techniques in image processing for its mathematical simplicity and accuracy for images that have low levels of noise. Bayesian rule is applied to the relationship between pixel intensities and class labels and the Gaussian mixture model is completed using Otsu's method.

Figure 4.17 is the classified T_1 image of Figure 4.1 and Table 4.5 is the confusion matrix.

Table 4.5
T_1 image confusion matrix for ML classification.

	CSF	GM	WM
CSF	77.13	21.67	1.20
GM	9.25	63.74	27.01
WM	0.92	5.68	93.40

In Figure 4.18 the result of ML classification can be seen for T_2 image of Figure 4.6. Corresponding confusion matrix is Table 4.6.

Table 4.6
T_2 image confusion matrix for ML classification.

	CSF	GM	WM
CSF	64.44	24.02	9.53
GM	2.66	64.18	33.16
WM	0	2.98	97.02

It is obvious from Tables 4.5, 4.4, 4.5 and 4.6 that segmentation results follow the same trend. That is to say, both Otsu's method and ML classification yields better results for CSF with T_1 images while the situation is opposite for WM and GM segmentations.

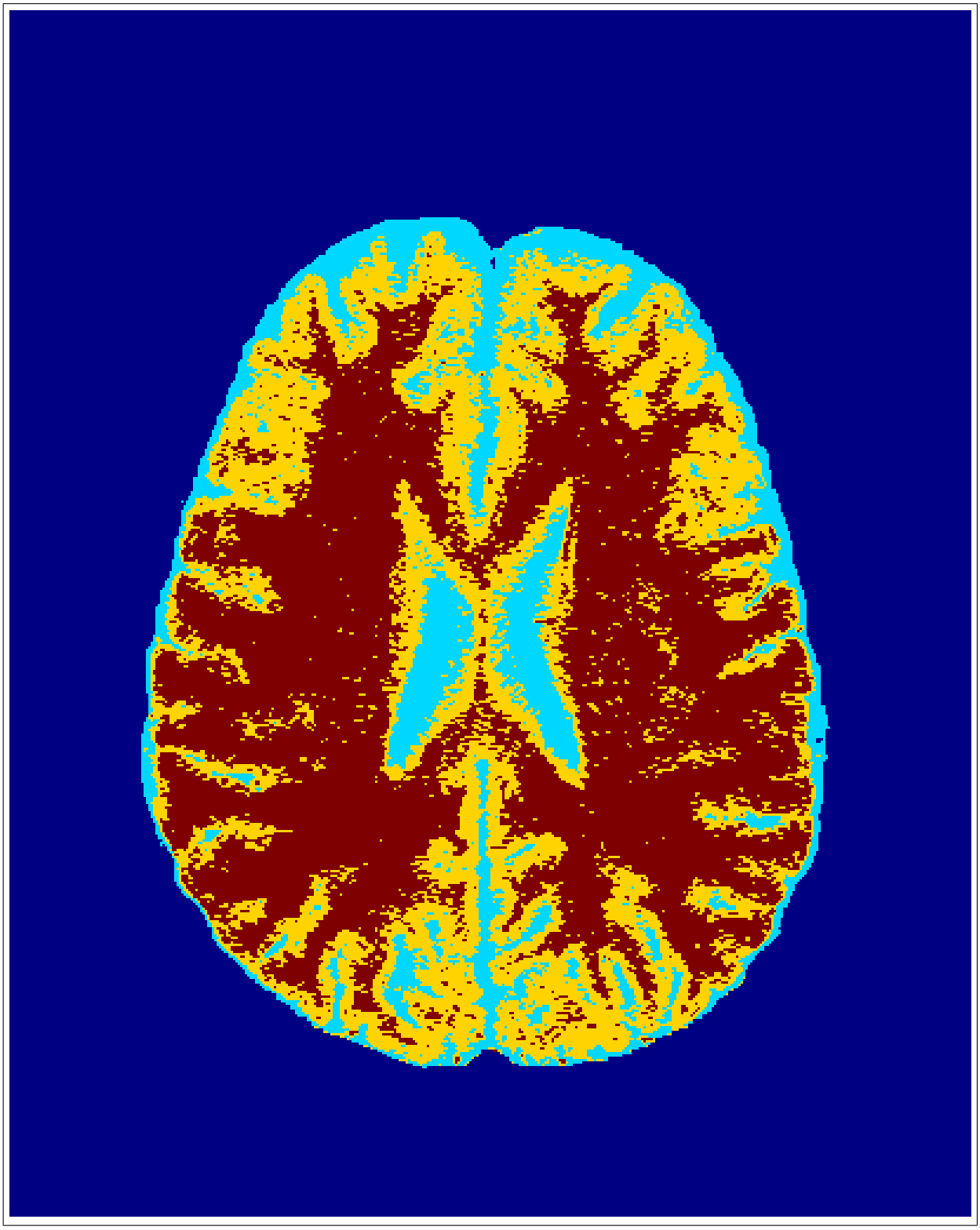

Figure 4.17 Segmented T_1 image using ML classification.

Figure 4.18 Segmented T_2 image using ML classification.

4.2.3 HMRF Segmentation

The images segmented above using Otsu's method and ML classification are now processed by a model-based classification scheme. HMRF theory incorporates likelihood of the class labels with the neighborhood configuration hence yielding a smoother and more accurate segmentation results. The result of HMRF approach for Figure 4.1 is given in Figure 4.19.

The smoothness of the result comparing to Figures 4.15 and 4.17 is obvious. The confusion matrix for Figure 4.19 is given in Table 4.7.

Table 4.7
T_1 image confusion matrix for HMRF segmentation.

	CSF	GM	WM
CSF	84.21	14.89	0.91
GM	12.49	63.73	23.78
WM	0.92	5.68	94.74

Again Figure 4.6 is processed with HMRF method and the resulting segmented image is given in Figure 4.20.

Corresponding confusion matrix can be seen in Table 4.8.

Table 4.8
T_2 image confusion matrix for HMRF segmentation.

	CSF	GM	WM
CSF	75.19	14.59	10.23
GM	5.50	60.38	34.13
WM	0.02	1.99	97.99

Analysis of confusion matrices 4.3, 4.5 and 4.7,it is clear that a great improvement in the segmentation of CSF volumes is achieved. On the other hand, segmentation

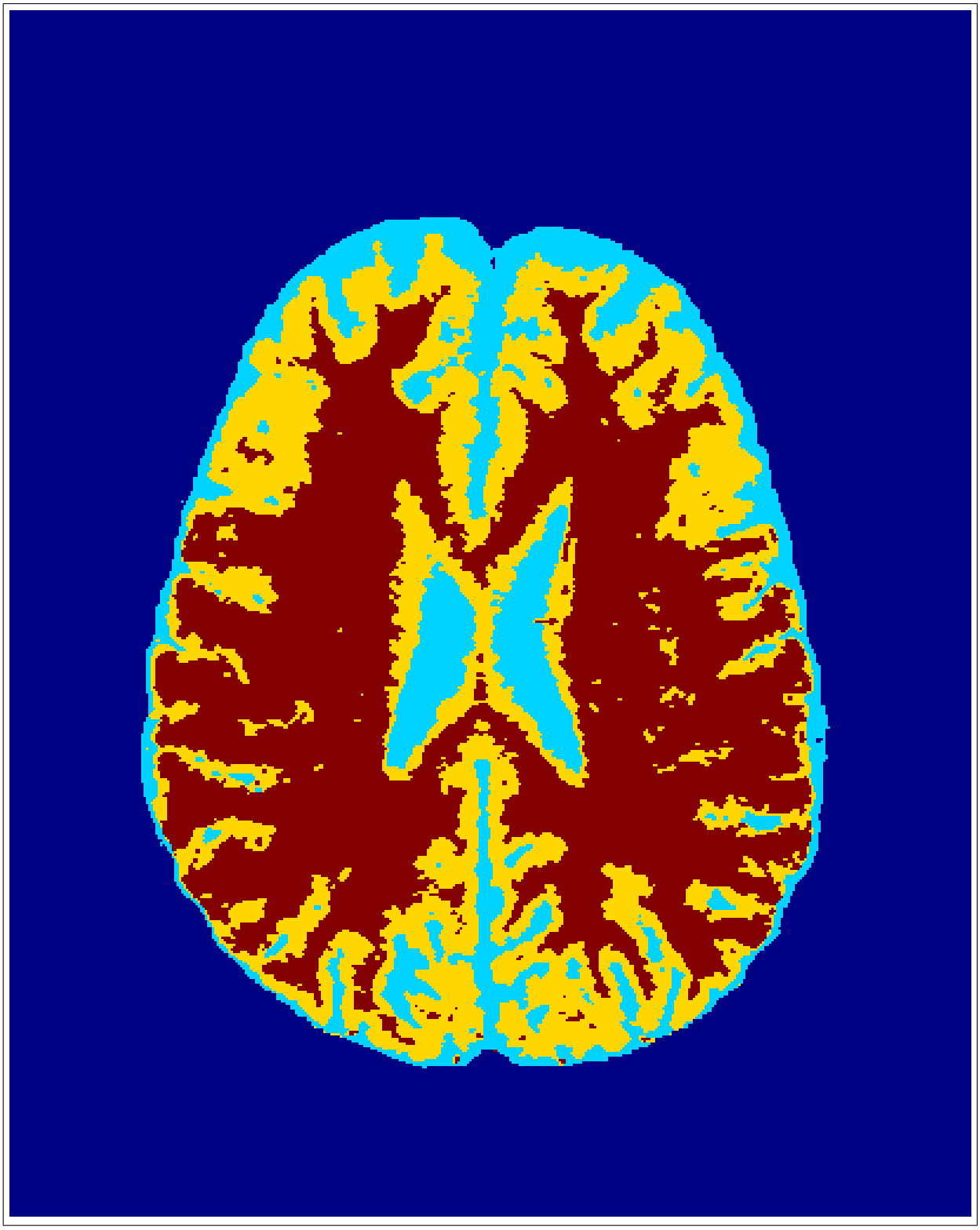

Figure 4.19 Segmented T_1 image with HMRF model.

Figure 4.20 Segmented T_2 image with HMRF model.

results for WM and GM do not differ too much. Again if confusion matrices for T_2 images are analyzed (Tables 4.4, 4.6 and 4.8) it can be concluded that the use of HMRF segmentation in image analysis greatly increases the accuracy of CSF classification while there is a slight improvement in WM extraction. However, there are more misclassified pixels in GM regions in MRF model relative to Otsu's method and ML.

4.3 $2D$ Segmentation

The theory of MR imaging suggests that pixel intensities in T_1 and T_2-weighted images are not linearly dependent to each other. In other words, using T_2-weighted images together with T_1-weighted ones provides more information about the location of the tissue types in the brain. These theoretical expectations were completely fulfilled by the results obtain in previous sections. For Otsu's method and ML classification, T_1-weighed images yield relatively good results for CSF classification and T_2-weighted images provided WM and GM information. MRF segmentation on the other hand offered better results for both CSF and GM while T_2-weighted images provided 98% success on segmentation. Using the aforementioned results in a multivariate ($2D$) segmentation scheme, thus, is expected to end up with further improvements in tissue classification. In the next subsections segmentation results of MR images in a $2D$ classification scheme are given for both ML and HMRF models.

4.3.1 ML Segmentation

For the $2D$ ML classification of three main tissues in the brain, Eq 3.37 is used as posterior distribution. Gaussian parameters are calculated, again, using Otsu's method and a numerically stable subroutine was written for the calculation of covariance matrices. Segmentation result of Figures 4.1 and 4.6 is given in Figure 4.21.

The confusion matrix of Figure 4.21 can be seen in Table 4.9.

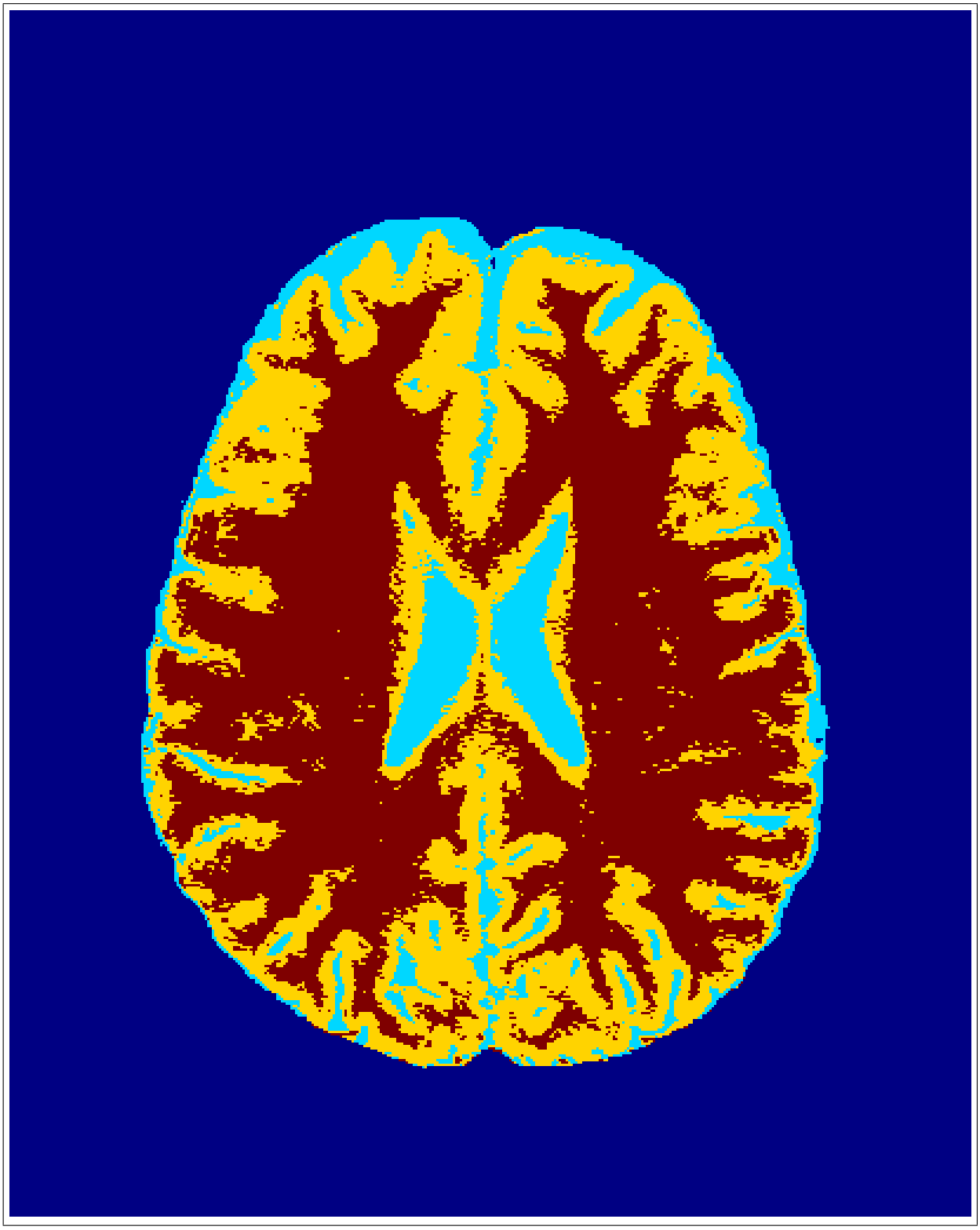

Figure 4.21 Segmented T_1-T_2 image with ML.

Table 4.9
$T1$-T_2 image confusion matrix for ML classification.

	CSF	GM	WM
CSF	77.49	22.31	0.19
GM	3.57	71.17	25.25
WM	0.74	2.26	97.00

As can be seen from Table 4.9, this $2D$ segmentation provides a great improvement in GM classification, in which other $1D$ schemes gave poor results. Moreover, the results for CSF classification resulted in better results (excluding MRF segmentation used for T_1-weighed images) and are almost the best for WM detection up to now.

4.3.2 HMRF Segmentation

This section covers the results of the ultimate segmentation scheme, namely multivariate HMRF model based segmentation. The final segmentation result is given in Figure 4.22 and the confusion matrix in Table

Table 4.10
$T1$-T_2 image confusion matrix for HMRF classification.

	CSF	GM	WM
CSF	80.00	20.03	0.05
GM	3.85	73.00	23.20
WM	0.99	1.41	98.00

Confusion matrix 4.10 shows that multivariate HMRF segmentation of MR images provides the best results for GM and WM discrimination while the classification rate for CSF is the second most successive one after the $1D$ MRF scheme for T_1 images.

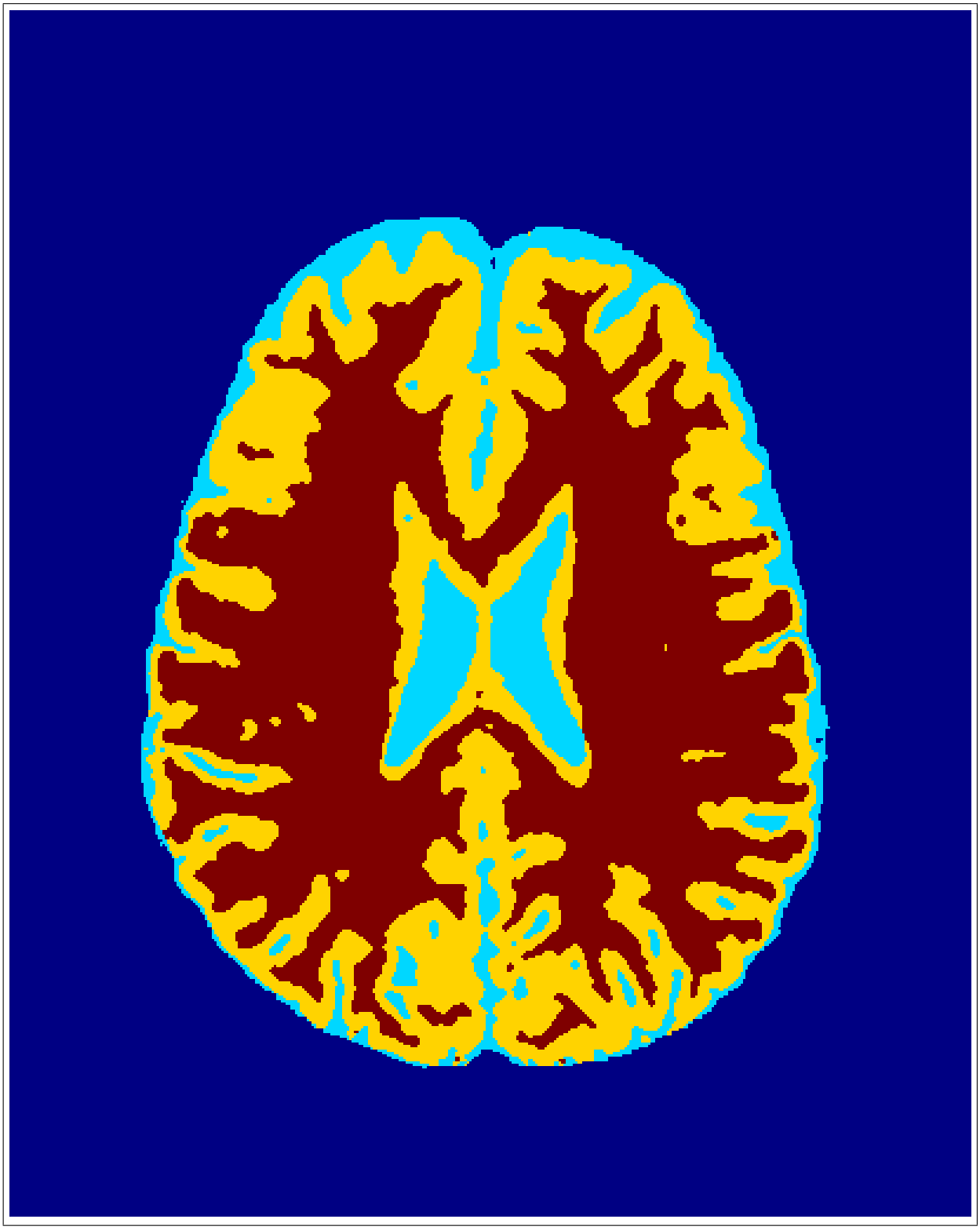

Figure 4.22 Segmented T_1-T_2 image with HMRF model.

5. CONCLUSION

Brain MR image segmentation is one of the most important post-processing applications in the field of medical imaging. It has a great importance because an appropriate computer guided surgical planning and surgery as well as treatment progress and diagnosis of some neurological diseases rely extensively on accurate classification of three main tissue types in the brain, namely CSF, GM and WM.

The literature offers a number of image processing techniques in order to segment brain MR images such as histogram based methods, edge detection algorithms, clustering methods, region growing methods, etc. However, considering the nature of brain images, model-based statistical approaches become the most favorable ones among all. That is because brain MR images are simple in nature and contrast regions corresponding to different tissues are piecewise constat. In other words, neglecting the noise and the RF inhomogeneity present in the image, one expects a constant contrast for each tissue in the brain. However, that is not the case in practice. First of all, all data gathered from the subject contains some amount of noise which affects the image negatively. But more importantly, all MR images suffer from another degradation effect, namely the bias field or RF inhomogeneity which in some cases greatly reduces the image quality. Bias field in images shows its deprecating effect up in automatic post-processing applications. In many cases, computer becomes incapable of differentiating some tissue regions resulting in misclassified pixels. In the literature one can find a number of techniques which try to extract the bias field from the image hence resulting in a more appropriate histogram for automatic detection. Some of these methods model the inhomogeneity as a multiplicative Gaussian field while some use non-parametric techniques. A novel approach addressing the bias field distortion is presented in [11]. In this approach the same slice of the brain is scanned for a total of eight times and the resulting pixel intensities are fitted to curves of Eq.s 2.10 and 2.11 for T_1 and T_2-weighted images respectively. Obtained $True - T_1$ and $True - T_2$ images then segmented in a multimodal ML classification algorithm according to Eq. 3.37.

Although the method provides the best segmentation results in the literature, it has some serious drawbacks. The main disadvantage of the method is the time required to gather such huge amounts of data. For some cases the patient is required to stay inside the machine for two to three hours. Apart from the discomfort to the subject, the method greatly increases the expenses as the number of scans per slice increases to eight. Moreover, the time spent inside the core brings another problem with it, motion artifacts. This in turn requires a registration process in order to eliminate motion between scans before the application of curve fitting algorithms, which is an extra computational burden.

In this study, we proposed a novel multimodal approach addressing the aforementioned drawbacks. To be more specific, the method aims to obtain comparable segmentation results by using two, not linearly dependent, images for more information and neighborhood relations of pixels in the images. By doing so scan time is reduced greatly by just taking two images per slice, one T_1 and one T_2-weighted, and bias field effect is tried to be compensated in some degree with the help of local statistics. Gaussian mixture model was adopted for the brain and MRF's were used to model local statistics of pixels.

In the first part of the analysis, after obtaining the multivariate segmentation of true parameter images, individual $True - T_1$ and $True - T_2$ images were analyzed with the help of confusion matrices. Assuming Figure 4.11 as golden truth, confusion matrices were constructed via a small subroutine. Looking at Tables 4.1 and 4.2, it can be said that $True - T_1$ images provide a good GM and WM discrimination while $True - T_2$ images gives better results on CSF and WM segmentations. Using these two true parameter images in a $2D$ segmentation scheme provides the ultimate, highly accurate segmentation results. The fact that the method in [11] provides the best results for tissue classification comes from its success on the almost complete elimination of bias field artifact.

Secondly, individual T_1 and T_2 images were processed using three widely used segmentation algorithms in a $1D$ classification scheme. Otsu's method, which gives

the optimum thresholds for gray scale images, was used in segmentation as well as to provide necessary initial parameters estimates for ML and MRF classification. Comparing Tables 4.3 and 4.4, it is easy to say thatT_1-weighted images are again good at CSF extraction while T_2-weighted images are better at GM and WM segmentations. That is exactly the same situation for ML estimates. Moreover, the improvement on CSF classification is obvious when ML estimation is used instead of Otsu's method. However, there were no significant improvements on WM discrimination when ML is used for segmentation both with T_1 and T_2-weighted images. On the other hand, the best result for WM classification was obtained when ML was used with T_2-weighted MR images. Comparing MRF with ML and Otsu on T_1-weighted images reveals that MRF results in the best CSF and WM differentiations, while there were no significant improvement on GM segmentation. CSF and WM detection using MRF with T_2 images was again the best while in that case, we misclassified around 5% more GM tissue.

For the last part of the analysis, as a novel approach, $2D$ segmentation of weighted images were obtained both for ML and MRF techniques. Looking at Table 4.9 one can conclude that all three tissue types were classified correctly with a higher accuracy compared to all $1D$ schemes. Especially the improvement on GM segmentation is obvious. Going further, the proposed method: segmentation of brain MR images using HMRF in a $2D$ segmentation scheme, provided the best results ever obtained as it was expected. Comparing Table 4.10 with other confusion matrices, it is obvious that the results as a whole improved greatly yielding comparable segmentations while eliminating the aforementioned drawbacks of other classification algorithms.

Although giving comparable segmentation results, the method still lacks high accuracy especially on CSF and GM classification. Hence, as a future work, any of the bias field extraction methods can be adopted and combined with expectation maximization algorithm in order to get better results. Using a *maximum a posteriori* criteria on bias field and calculating the most probable bias field in each iteration, the complete bias field can be extracted from the image gradually in each iteration resulting in a more accurate segmentation result.

APPENDIX A. LEVENBERG - MARQUARDT ALGORITHM

The Levenberg - Marquardt algorithm provides a numerical solution to the problem of minimizing a function, which is generally a nonlinear one, over a space of parameters of the function.

A.1 The Problem

Given a set of empirical data pairs, (x_i, y_i) optimize the parameters β of the model curve $f(x_i, \beta)$ so that the sum of the squared errors

$$S(\beta) = \sum_{i=1}^{m} [y_i - f(x_i, \beta)]^2 \tag{A.1}$$

becomes minimal.

A.2 The Solution

The Levenberg - Marquardt is an iterative optimization algorithm. To start a minimization, the user has to make some initial guess for the parameter vector β. In many cases, an uninformed initial value for the parameter vector as $\beta = (1, 1, 1, ..., 1)$ will work fine while for other cases the algorithm converges only if the initial guess is already close to the final solution.

In each iteration step, the parameter vector β, is replaced by a new estimate, $\beta + \sigma$. To determine σ, the functions $f(x_i, \beta + \sigma)$ are approximated by their linearizations;

$$f(x_i, \beta + \sigma) \approx f(x_i, \beta) + J_i \sigma, \tag{A.2}$$

where;

$$J_i = \frac{\partial f(x_i, \beta)}{\partial \beta}, \tag{A.3}$$

is the gradient of f with respect to β.

At a minimum of sum of the squares, called S, the gradient of S with respect to β is 0. Differentiating the the squares in the defination of S, using the first-order approximation in Eq. A.2 and setting the result to zero leads to;

$$(J^T J\sigma) = J^T[y - f(\beta)], \tag{A.4}$$

where J is the Jacobian matrix whose i^{th} row equal J_i, and where y and f are vectors with i^{th} component y_i and $f(x_i, \beta)$, respectively. This is a linear set of equations which can be solved for σ.

Levenberg's contribution is the replacement of this equation by a damped version;

$$(J^T J + \lambda I)\sigma = J^T[y - f(\beta)], \tag{A.5}$$

where I is the identity matrix. The damping factor λ is adjusted in each iteration.

"Levenberg's algorithm has the disadvantage that if the value of the damping factor is large, inverting $(J^T J + \lambda I)$ is not used at all. Marquardt provided the insight that we can scale each component of the gradient according to the curvature so that there is larger movement along the directions where the gradient is smaller. This avoids slow convergence in the direction of small gradient. Therefore Marquardt replaced the identity matrix with the diagonal of the Hessian matrix, $J^T J$, resulting the Levenberg

- Marquardt algorithm [20]."

$$(J^T J + \lambda diag(J^T J))\sigma = J^T[y - f(\beta)]. \tag{A.6}$$

APPENDIX B. OTSU THRESHOLDING

An image is a $2D$ grayscale intensity function and contains N pixels with gray levels from 1 to L. The number of pixels with gray level i is denoted f_i, giving a probability of gray level i in an image of

$$p_i = f_i/N. \tag{B.1}$$

In the case of bi-level thresholding of an image, the pixels are divided into two classes, C_1 with gray levels $[1, 2, ..., t]$ and C_2 with gray levels $[t+1, t+2, ..., L]$. Then, the gray level probability distributions for the two classes are;

$$\begin{aligned} C_1 &: p_1/\omega_1(t), ..., p_t/\omega_1(t), \\ C_2 &: p_{t+1}/\omega_2(t), ..., p_L/\omega_2(t), \end{aligned} \tag{B.2}$$

where $\omega_1(t) = \sum_{i=1}^{t} p_i$ and $\omega_2(t) = \sum_{i=t+1}^{L} p_i$.

Also the means for classes C_1 and C_2 are;

$$\begin{aligned} \mu_1 &= \sum_{i=1}^{t} i p_i/\omega_1(t), \\ \mu_2 &= \sum_{i=t+1}^{L} i p_i/\omega_2(t). \end{aligned} \tag{B.3}$$

Let μ_T be the mean intensity for the whole image. It is easy to show that;

$$\begin{aligned} \omega_1\mu_1 + \omega_2\mu_2 &= \mu_T, \\ \omega_1 + \omega_2 &= 1. \end{aligned} \tag{B.4}$$

Using discriminant analysis, Otsu defined the between-class variance of the thresholded image as;

$$\sigma_B^2 = \omega_1(\mu_1 - \mu_T)^2 + \omega_2(\mu_2 - \mu_T)^2. \tag{B.5}$$

For bi-level thresholding, Otsu verified that the optimal threshold t^* is chosen so that the between-class variance σ_B^2 is maximized; that is,

$$t^* = arg\max_t \sigma_B^2(t), \quad 1 \leq t < L. \tag{B.6}$$

The formula Eq. B.6 can be easly extended to multilevel thresholding of an image [19]. Assuming that there are $M-1$ thresholds, $\{t_1, t_2, ..., t_{M-1}\}$, which divide the original image into M classes: C_1 for $[1, ..., t_1]$, C_2 for $[t+1, ..., t_2]$, ..., C_i for $[t_{i-1}+1, ..., t_i]$, ..., and C_M for $[t_{M-1}+1, ..., L]$, the optimal thresholds $\{t_1^*, t_2^*, ..., t_{M-1}^*\}$ are chosen by maximizing σ_B^2 as follows;

$$\{t_1^*, t_2^*, ..., t_{M-1}^*\} = arg\max\{\sigma_B^2(t_1, t_2, ..., t_{M-1})\}, \quad 1 \leq t_1 < .... < t_{M-1} < L, \tag{B.7}$$

where;

$$\begin{aligned} \sigma_B^2 &= \sum_{k=1}^{M} \omega_k(\mu_k - \mu_T)^2, \\ \omega_k &= \sum_{i \in C_k} p_i, \\ \mu_k &= \sum_{i \in C_k} i p_i / \omega(k). \end{aligned} \tag{B.8}$$

REFERENCES

1. Atkins, M. S., and B. T. Mackiewich, "Fully automatic segmentation of the brain in mri," *IEEE Transactions on Medical Imaging*, Vol. 17, pp. 98–108, Feb 1998.

2. Zhang, Y., M. Brady, and S. smith, "Segmentation of brain mr images through a hidden markov random field model and the expectation-maximization algorithm," *IEEE Transactions on Medical Imaging*, Vol. 20, pp. 45–57, Jan 2001.

3. Brummer, M. E., "Optimized intensity thresholds for volumetric analysis of magnetic resonance imaging data," *Proc. SPIE*, Vol. 1808, pp. 29–310, 1992.

4. Kundu, A., "Local segmentation of biomedical images," *Comp. Med. Imag. Graph.*, Vol. 14, pp. 173–183, 1990.

5. Bishop, C. M., *Neural Networks For Pattern Recognition*, Oxford, UK: Oxford Uni., 1995.

6. Guillemaud, R., and J. M. Brady, "Estimating the bias field of mr images," *IEEE Transactions on Medical Imaging*, Vol. 16, pp. 238–251, Jun 1997.

7. Wells, W. M., E. L. Grimson, R. Kikinis, and F. A. Jolesz, "Adaptive segmentation of mri data," *IEEE Transactions on Medical Imaging*, Vol. 15, pp. 429–442, Aug 1996.

8. Geman, S., and D. Geman, "Stochastic relaxation, gibbs distributions and bayesian restoration of images," *IEEE Transactions Pattern Anal. Machine Intell.*, Vol. 6, pp. 721–741, Jun 1984.

9. Fischl, B., D. H. Salat, E. Busa, M. Albert, M. Dieterich, C. Haselgrove, A. Kouwe, R. Killiany, D. Kennedy, S. Klaveness, A. Montillo, N. Makris, B. Rosen, and A. M. Dale, "Whole brain segmentation: Automated labeling of neuroanatomical structures in the human brain," *Neuron*, Vol. 33, pp. 341–355, Jan 2002.

10. Chen, T., and T. S. Huang, "Region based hidden markov random field model for brain mr image segmentation," *Proceedings of World Academy of Science, Engineering and Technology*, Vol. 4, pp. 233–236, Feb 2005.

11. Agus, O., "Elimination of signal intensity artifacts in segmentation," Master's thesis, Bogazici University, Istanbul, Turkey, 2008.

12. Vovk, U., F. Pernus, and B. Likar, "Mri intensity inhomogeneity correction by combining intensity and spatial information," *Phys. Med. Biol.*, Vol. 49, pp. 4119–4133, Aug 2004.

13. Besag, J., "On the statistical analysis of dirty pictures(with discussion)," *J. of Royal Statist. Soc.*, Vol. 48, no. 3, pp. 259–302, 1986.

14. Li, S. Z., *Markov Random Field Modeling in Computer Vision*, Berlin, Germany: Springer-Verlag, 1995.

15. Besag, J., "Spatial interaction and the statistical analysis of lattice systems(with discussion)," *J. of Royal Statist. Soc.*, Vol. 36, no. 2, pp. 192–326, 1974.

16. Dempster, A. P., N. M. Laird, and D. B. Bubin, "Maximum likelihood from incomplete data via em algorithm," *J. of Royal Statist. Soc.*, Vol. 39, no. 1, pp. 1–38, 1977.

17. Junxi, S., "Bayesian image segmentation based on an inhomogeneous hidden markov random field," *Proceedings of the ICPR'04, IEEE*, 2004.

18. Otsu, N., "A threshold selection method from gray-level histograms," *IEEE Transactions on Systems, Man and Cybernetics*, Vol. 9, pp. 62–66, Jan 1979.

19. Liao, P. S., T. S. Chen, and P. C. Chung, "A fast algorithm for multilevel thresholding," *J. Inf. Sci. Eng*, Vol. 17, no. 2, pp. 713–727, 2001.

20. Marquardt, D. W., "An algorithm for least squares estimation of nonlinear parameters," *Journal of the Society for Industrial and Applied Mathematics*, Vol. 11, pp. 431–441, Jun 1963.